

Simultaneous *Chandra* and *HST* observations of the quiescent neutron-star low-mass X-ray binaries in 47 Tucanae

M. van den Berg,^{1*} L.E. Rivera Sandoval,² C.O. Heinke,³ H.N. Cohn,⁴ P.M. Lugger,⁴ J.E. Grindlay,¹ P.D. Edmonds,¹ J. Anderson,⁵ A. Catuneanu^{3,6}

¹Center for Astrophysics | Harvard & Smithsonian, 60 Garden Street, Cambridge, MA 02138, USA

²Department of Physics and Astronomy, University of Texas Rio Grande Valley, Brownsville, TX 78520, USA

³Department of Physics, University of Alberta, CCIS 4-183, Edmonton, AB, T6G 2E1, Canada

⁴Department of Astronomy, Indiana University, 727 E. Third St, Bloomington, IN 47405, USA

⁵Space Telescope Science Institute, 3800 San Martin Drive, Baltimore, MD 21218, USA

⁶Dana Canada Corporation, 656 Kerr Street, Oakville, ON L6K 3E4, Canada

Accepted XXX. Received YYY; in original form ZZZ

ABSTRACT

We present simultaneous *Chandra* X-ray Observatory and *Hubble Space Telescope* observations of three certain (X5, X7, W37) and two likely (X4, W17) quiescent neutron-star low-mass X-ray binaries (qLMXBs) in the globular cluster 47 Tuc. We study these systems in the X-ray, optical and near-ultraviolet (NUV) using the simultaneous data and additional non-contemporaneous *HST* data. We have discovered a blue and variable NUV counterpart to W17. We have not securely identified the eclipsing qLMXB W37 in the optical or NUV. Deeper high-resolution imaging is needed to further investigate the faint NUV excess near the centre of the W37 error circle. We suggest that a previously identified optical astrometric match to X7 is likely the true counterpart. The H α emission and the location of the counterpart in the colour-magnitude diagram, indicate that the secondary is probably a non-degenerate, H-rich star. This is consistent with previous results from fitting X7's X-ray spectrum. In X4, the simultaneous X-ray and optical behaviour supports the earlier suggestion that the X-ray variability is driven by changes in accretion rate. The X-ray eclipses in X5 coincide with minima in the optical/NUV light curves. Comparison of the 47 Tuc qLMXBs with the cataclysmic variables (CVs) in the cluster confirms that overall the qLMXBs have larger X-ray-to-optical flux ratios. Based on their optical/NUV colors, we conclude that the accretion disks in the qLMXBs are less prominent than in CVs. This makes the ratio of X-ray flux to excess blue optical flux a powerful discriminator between CVs and qLMXBs.

Key words: globular clusters: individual: 47 Tuc (NGC 104) – X-rays: binaries – binaries: close – stars: neutron

1 INTRODUCTION

Low-mass X-ray binaries (LMXBs) consist of a neutron star or black hole that accretes from a low-mass ($\lesssim 1 M_{\odot}$) companion. Most known LMXBs are transient systems in which the X-ray luminosity can change by orders of magnitude when they switch from an actively accreting state to a quiescent, low-accretion rate state (or the other way around). The majority of LMXBs are believed to be quiescent most of the time. In neutron-star systems, quiescence can offer a glimpse of the accretor: the quiescent X-ray emission may feature a soft thermal component, thought to be radiated by the neutron-star surface through the release of heat that is deposited during episodes of accretion (Brown et al. 1998). Harder non-thermal

emission can contribute to the X-rays as well; its origin is not well understood, but suggestions include synchrotron shock emission or low-level residual accretion (Campana et al. 1998, Bernardini et al. 2013). Since the population of LMXBs is concentrated towards the Galactic bulge, observations of quiescent LMXBs (qLMXBs) with typical X-ray luminosities of $L_X \approx 10^{31-33} \text{ erg s}^{-1}$ are often impeded by high levels of extinction. As a result, quiescent systems can be difficult to find or recognize.

It has been known since the early seventies (Katz 1975) that a good place to look for luminous LMXBs is in globular clusters, where stellar encounters add new pathways to their formation. Thanks to the sensitivity and spatial resolution of the *Chandra* X-ray Observatory, the number of quiescent LMXBs in globular clusters was also found to be correlated with encounter rate (e.g. Heinke et al. 2003b, Pooley et al. 2003, Pooley & Hut 2006). Due to their

* E-mail: mvandenberg@cfa.harvard.edu

Table 1. Summary of *HST* observations analyzed in this work

Program	Instrument	Start observations	End observations	Filter	N_{exp}	T_{exp} (s)	Comments
GO 9019	ACS/HRC	2002–Apr–12 22:48	2002–Apr–13 17:51	F220W	11	1870	
				F330W	8	528	
				F435W	12	720	
				F475W	5	300	
GO 9443	ACS/WFC	2002–Jul–07 22:30	2002–Jul–07 22:32	F435W	1	150	
GO 9281	ACS/WFC	2002–Sep–30 01:35	2002–Sep–30 06:24	F435W	3	300	overlaps with <i>Chandra</i> ObsID 2735; analyzed by us but also in HUGS
				F625W	8	465	
				F658N	7	2630	
		2002–Oct–02 20:47	2002–Oct–03 00:43	F435W	4	310	overlaps with <i>Chandra</i> ObsID 2737
				F625W	7	455	
				F658N	7	2630	
		2002–Oct–11 02:16	2002–Oct–11 10:12	F435W	3	345	overlaps with <i>Chandra</i> ObsID 2738
				F625W	7	400	
				F658N	6	2180	
GO 10775	ACS/WFC	2006–Mar–13 01:42	2006–Mar–13 05:24	F606W	5	203	in HUGS
				F814W	5	203	
GO 11729	WFC3/UVIS	2010–Sep–28 23:28	2010–Sep–29 00:07	F336W	3	1190	in HUGS
GO 12311	WFC3/UVIS	2010–Nov–21 11:59	2010–Nov–22 19:34	F275W	14	4822	in HUGS
GO 12971	WFC3/UVIS	2012–Nov–14 10:45	2013–Sep–20 10:09	F336W	20	12050	in HUGS
GO 12950	WFC3/UVIS	2013–Aug–13 02:10	2013–Aug–13 11:01	F300X	24	14576	in HUGS
				F390W	8	4624	

The listed start and end times of the observations (in UTC) delineate the time span that is covered by the specified exposures. For each filter, N_{exp} is the number of images and T_{exp} is the total exposure time.

dynamical origin, it is not obvious that globular-cluster (q)LMXBs can serve as a proxy for the field population. For example, in regard to their orbital periods, it has been suggested that ultra-compact systems (i.e. those with periods $\lesssim 80$ min) are more common among cluster LMXBs, possibly a signature of their different formation scenarios (Deutsch et al. 2000). Concerning their X-ray emission, it has been found that the X-ray spectra of many cluster qLMXBs are dominated by the soft and steady thermal component, and lack the additional harder (and in many cases variable) non-thermal component that is often seen in field qLMXBs¹ (Walsh et al. 2015, Bahramian et al. 2015). Small sample sizes and selection biases may (partly) explain these apparent differences. We know of fewer than two dozen (transient or persistently bright) LMXBs in globular clusters, as well as a similar number of qLMXBs that are bright enough for an X-ray spectral or variability study. LMXBs are typically discovered when they go in outburst, but in clusters that are targeted with deep *Chandra* pointings, LMXBs are also first identified in quiescence by their distinct soft spectra. These separate discovery methods may select systems with very different outburst histories or duty cycles. Detailed studies of field and cluster systems can help clarify to what extent the observed properties really signify different underlying populations.

Another motivation for studying neutron-star qLMXBs is that fitting their thermal X-ray emission with a suitable model can provide mass and radius constraints when combined with a distance estimate (Rutledge et al. 2002). Since the mass-radius relation is

determined by the neutron-star equation of state, spectral fitting has become one of the main methods to place limits on the equation of state of cold dense matter (see e.g. Özel & Freire 2016). The details of the adopted model depend on the composition of the neutron-star atmosphere. This composition in turn is determined by the nature of the mass donor: accretion supplies fresh material to the outer layers of the neutron star, which quickly stratifies with the lightest elements settling on top (Romani 1987, Alcock & Illarionov 1980). Main-sequence donors give rise to Hydrogen (H) rich atmospheres, while material accreted from white-dwarf donors in ultra-compact systems is rich in Helium, Carbon, and/or Oxygen. If the atmospheric composition is unknown, this introduces systematic uncertainties in the mass and radius estimates (Servillat et al. 2012, Echiburú et al. 2020). Another complication arises when the X-ray spectrum is not purely thermal. To investigate whether accretion could “contaminate” the spectrum, variability in X-rays or at other wavelengths can be used as a diagnostic. Identifying the nature and properties of the optical or near-ultraviolet (NUV) counterpart can be crucial for inferring the composition of the neutron-star atmosphere or to check for ongoing accretion (see e.g. Haggard et al. 2004, Heinke et al. 2014).

Finally, the non-thermal component of the X-ray emission also provides an opportunity to study accretion physics at low mass accretion rates. Accretion has been considered a likely origin of the non-thermal component (Campana et al. 1998), supported by the agreement of its spectral shape with a bremsstrahlung model (Chakrabarty et al. 2014). Accretion is likely also responsible for a portion of the thermal spectrum, evidenced by correlated variability in both components (Campana et al. 2004; Cackett et al. 2010; Wijnands et al. 2015). Different scenarios have been pro-

¹ The class of transitional millisecond pulsars is an exception, see e.g. Linares (2014).

posed to explain the emergent spectrum in Cen X-4 and other weakly magnetic systems. D’Angelo et al. (2015) discuss a model where the emission largely originates in a boundary layer close to the neutron-star surface, and constrain the properties of this layer and the dominant radiation mechanism. Qiao & Liu consider the radiative coupling between the thermal (from the neutron-star surface) and non-thermal (from the accretion flow) emission, and find that only a small fraction of the energy transferred to the neutron star needs to be thermalized and scattered back to the—radiatively inefficient—accretion flow to explain the observations (Qiao & Liu 2018, Qiao & Liu 2020, Qiao & Liu 2021). Knowing the conditions in and around the accretion region is also important to understand the observed mass-donor properties (e.g. Shahbaz et al. 2022).

The massive globular cluster 47 Tuc (NGC 104) hosts at least three certain and two probable neutron-star qLMXBs, none of which have ever been caught in outburst. These are, respectively, X5 (also known as W58), X7 (also known as W46) and W37; and the candidates X4 (also known as W125) and W17. The ROSAT sources X5 and X7 were already identified as likely qLMXBs (also called soft X-ray transients) by Hasinger et al. (1994), and their nature was confirmed by the first *Chandra* studies of the cluster (Grindlay et al. 2001, Heinke et al. 2003a). The *Chandra* sources W37 and W17, and the ROSAT source X4 were added as (candidate) qLMXBs by Heinke et al. (2005a). X4 and W17 are notable because, unlike in many other cluster qLMXBs, their X-ray spectra feature prominent non-thermal emission, suggesting that accretion may be happening at a very low rate. X5 and especially the extremely stable source X7 are among the best-studied cluster qLMXBs, for several reasons. They are bright in X-rays, and their spectra contain no discernible non-thermal components (Heinke et al. 2006; Bogdanov et al. 2016). Moreover, 47 Tuc suffers from little foreground extinction and its distance is precisely determined. From the known orbital periods of X5 (8.667 hr) and W37 (3.087 hr), we know that their neutron-star atmospheres must be H-rich.

In this paper we study these five (candidate) qLMXBs in the X-ray, optical and NUV. We investigate the known optical counterparts to X5, which was found and studied in detail by Edmonds et al. (2002a), and to X4, which was briefly reported in Beccari et al. (2014). We look for counterparts to the three others, which so far have not been identified in the optical or NUV. Our study is based on data from several *Hubble Space Telescope* (*HST*) programs, including images from the Advanced Camera for Surveys (ACS) that were taken simultaneously with deep *Chandra* observations of 47 Tuc. This allows us to study correlated X-ray/optical behavior in our sources. There is a sixth source in 47 Tuc that is also believed to be an LMXB, viz. X9 (W42). It has been suggested that the accretor in this ultra-compact system is a black hole, although a neutron-star primary cannot be excluded. Details can be found in Miller-Jones et al. (2015), Bahramian et al. (2017), Church et al. (2017), and Tudor et al. (2018).

For the cluster reddening, we assume $E(B - V) = 0.04 \pm 0.02$ (Salaris et al. 2007). Following Bogdanov et al. (2016) who calculated the weighted mean of published distances to 47 Tuc, we adopt a distance to the cluster of $4.53^{+0.08}_{-0.04}$ kpc. This average does not include the Gaia DR2 estimate (Chen et al. 2018), but at $4.45 \pm 0.01 \pm 0.12$ kpc (random and systematic errors, respectively) the latter is consistent with our adopted value. We start with an overview of the observations in Section 2, followed by a description of the data reduction and analysis in Section 3. In Section 4 we present our findings, which we discuss in the broader context of other globular-cluster qLMXBs, and other faint cluster X-ray sources in Section 5.

2 OBSERVATIONS

2.1 Simultaneous X-ray and optical observations

We observed 47 Tuc simultaneously with *Chandra* and *HST* on 2002 September 30, October 2–3, and October 11. This temporal spacing was chosen to sample variability on timescales from hours to weeks. The *HST* data were taken with the Wide Field Channel (WFC) on ACS under program GO 9281. The two CCD detectors of the WFC give a combined field of view of $3.4' \times 3.4'$ with a $2.5''$ gap in the middle. We obtained images through a blue (F435W), red (F625W) and narrow-band $H\alpha$ (F658N) filter for total exposure times of 955 s, 1320 s, and 7440 s, respectively. During each of the three visits, we obtained exposures in all three filters; this way, we were able to construct quasi-instantaneous colours that represent the stars’ actual colours as closely as possible, minimizing the effects of variability. In the crowded fields of globular clusters, this filter choice has proven to be efficient in separating the true optical counterparts of *Chandra* sources from optical sources that happen to lie in the X-ray error circles by chance (see e.g. Cohn et al. 2010, Luggner et al. 2017). Accreting binaries with low-mass donors typically have strong $H\alpha$ emission lines superposed on a blue continuum coming from an accretion disk or stream (or, in the case of cataclysmic variables (CVs), from the white dwarf as well), while the stars in magnetically active binaries with enhanced coronal X-ray emission can show chromospheric $H\alpha$ emission lines. For each filter, we employed a dither pattern with fractional-pixel offsets so that the native detector resolution of $0.05''$ per pixel could be improved when combining the individual images. A summary of the GO 9281 exposures can be found in Table 1.

The *Chandra* exposures that overlap with the *HST* observations are part of a larger data set that consists of four pairs of ACIS-S exposures, each pair made up of a long (~ 65 ks) full-frame exposure (ObsIDs 2735–2738) and a short (~ 5 ks) sub-array exposure (1/4 of an ACIS chip; ObsIDs 3384–3387). The *HST* data were taken during the first (ObsID 2735), third (ObsID 2737) and fourth (ObsID 2738) of the long exposures. Details of the entire 2002 *Chandra* data set of 47 Tuc and its analysis are given in Heinke et al. (2005b).

2.2 Additional *Chandra* data

We take the positions of the qLMXBs and the sources we use for registering the *Chandra* and *HST* astrometry (see Section 3.2.1) from the catalog of 47 Tuc *Chandra* sources by Bhattacharya et al. (2017). This deep source list is based on all ACIS-S data from 2002 described in the previous section, as well as ACIS-I data from 2000 and ACIS-S data from 2014–2015. The combined data represent 540 ks of exposure time on the cluster, with some parts receiving more exposure than others as a result of the use of different imaging modes (full-frame, 1/4 or 1/8 sub-array). Bhattacharya et al. (2017) applied the EDSEER algorithm (Li et al. 2004) to the event files, improving the spatial resolution and the ability to separate sources in the crowded cluster core. The 95% confidence radii on the positions in the catalog were calculated using the prescription by Hong et al. (2005), based on *wavdetect* runs on mock ACIS-I data.

2.3 Additional NUV and optical imaging with *HST*

We have analyzed NUV images of 47 Tuc from two *HST* programs. On 2013 August 13 we observed the cluster with the UVIS channel on the Wide Field Camera 3 (WFC3) as part of program GO 12950. UVIS covers a field of view of $2.7' \times 2.7'$ with a scale

ID	f_X ($\times 10^{-14}$) erg s $^{-1}$ cm $^{-2}$	$\log f_X/f_{U_{300}}$	$\log f_X/f_{B_{435}}$	epoch f_X
X4	4.3 \pm 1.5	2.1(2)	1.6(2)*	ObsID 2735–high
	2.4 $^{+0.5}_{-1.1}$	1.8(2)	1.7(2)*	other 2002 ObsIDs
X5	58 \pm 3	2.50(4)	2.13(3)	2000
X7	78 \pm 4	2.63(4)	2.04(3)	2000
W17	1.7 $^{+0.3}_{-0.5}$	0.9(1)	\geq 1.5	2000 and 2002 data
W37	7.4 $^{+0.8}_{-0.5}$	\geq 0.9	\geq 0.5*	ObsID 2735–high

Table 2. X-ray fluxes f_X and magnitudes U_{300} and B_{435} for the counterparts discussed in Sec. 4 are corrected for absorption. For X7, we assumed N1 as the counterpart. For W37, we used the magnitudes of star 4, the faintest neighbor, to compute limits on the flux ratio’s. The last column gives the epoch of the X-ray fluxes, where ‘ObsID 2735–high’ refers to the high-flux part of ObsID 2735 (different for X4 and W37). Flux ratios based on X-ray and optical measurements from the same epoch are marked with an asterisk (*). X-ray fluxes for X4 and W17 are given for the 0.5–10 keV band. For X5, X7 and W37 X-ray fluxes are given in the 0.5–2.5 keV band but due to their very soft spectra, the values match the 0.5–10 keV flux very well. A systematic error on the optical magnitude calibration of 2% (upper limit quoted in [Sirianni et al. 2005](#)) would add an error of ~ 0.2 to the flux ratios.

of 0.04'' per pixel. During two consecutive visits, 24 images were obtained through the F300X filter for a total exposure time of 14 576 s, and eight images were taken through the F390W filter for a total exposure of 4624 s. The dithering pattern included fractional-pixel offsets. More details can be found in [Rivera Sandoval et al. \(2015\)](#).

We also analyzed archival images of 47Tuc from program GO 9019 that were obtained with the ACS High Resolution Camera (HRC) on 2002 April 12–13. The HRC offers a relatively small field of view of 29'' \times 25'', but a superb detector scale of $\sim 0.025''$ per pixel. This data set comprises images taken through ten filters, which are laid out in a mosaic pattern covering the cluster centre. We only analyzed the exposures in the NUV and blue filters F220W, F330W, F435W (only the 60 s exposures) and F475W that include X7 and/or W37 in their field of view. The other three systems are not covered by this data set. Basic information for the GO 12950 and GO 9019 data that we used can be found in Table 1.

Finally, we use the star catalogs of 47Tuc from the *HST* UV Globular cluster Survey (HUGS; [Nardiello et al. 2018](#)). These are based on ACS/WFC F606W and F814W images from program GO 10775 (P.I. Sarajedini; [Sarajedini et al. 2007](#)) and ACS/WFC and WFC3/UVIS images in the filters F275W (GO 12311, P.I. Piotto), F336W (GO 11729, P.I. Holtzman; GO 12971, P.I. Richer), and F435W (GO 9443, P.I. King; GO 9281—which is our data set as described in Sect. 2.1). The HUGS images in the blue filters were taken over a time span of more than eleven years: F275W images are from 2010, F336W images from 2010–2013 and F435W images from 2002. This could impact the blue colours of stars if they are (long-term) variables. The F606W and F814W images were taken within a time span of <4 hours, so the derived red colour is only sensitive to short-term brightness variations. We refer to Table 1 for the start and end times of all 47 Tuc HUGS data. We have used the magnitudes extracted with the HUGS ‘‘method 3’’ photometry, which is appropriate for very crowded environments.

3 DATA REDUCTION AND ANALYSIS

3.1 X-ray data

We refer to [Heinke et al. \(2005a,b\)](#) and [Bhattacharya et al. \(2017\)](#) for details on the reduction of the *Chandra* data. We extracted light curves from the four long ACIS-S exposures from 2002 with time bins of 3000 s (X4, W17, W37) or 500 s (for X5 and X7, which are much brighter). Event times were converted to solar-system barycentre times using the CIAO tools. X-ray luminosities from earlier works ([Heinke et al. 2005a,b](#)) that assumed a cluster distance of 4.85 kpc, were adjusted for the distance we adopt here (4.53 kpc).

Neither X5 nor X7 show evidence for intrinsic X-ray luminosity variability. We use the unabsorbed X-ray fluxes that were derived from hydrogen-atmosphere spectral fits to the 2000 data in [Heinke et al. \(2003a\)](#). The count rate for X5 is variable, but (apart from the obvious eclipses) the variability appears to reflect changes in the amount of obscuration in front of the X-ray source, instead of changes in the intrinsic flux, as evidenced by the increased N_H fit in periods of lower countrate ([Heinke et al. 2003a](#); [Bogdanov et al. 2016](#)). The X5 observation from 2000 appears to be the least affected by obscuration. The adopted flux for W37 was taken from Table 3 of [Heinke et al. \(2005a\)](#), and reflects the results of fitting the spectrum extracted from the segment of ObsID 2735 that is least affected by absorption. The model used is a combination of an absorbed hydrogen atmosphere plus a non-thermal (power-law) component. The flux values for X5, X7 and W37 from [Heinke et al. \(2003a\)](#) and [Heinke et al. \(2005a\)](#) were computed for the 0.5–2.5 keV band, but the spectra are so soft, with no (X5, X7) or almost no (W37; $\lesssim 2\%$ flux contribution) power-law component, that these are consistent for the 0.5–10 keV band as well. W17 is not significantly variable. The spectrum from the 2000 and 2002 data can be fit with a combination of a hydrogen-atmosphere plus power-law model, with the latter the dominant component. We convert the total intrinsic luminosity in the 0.5–10 keV band from Table 2 in [Heinke et al. \(2005a\)](#) to an unabsorbed flux. The flux of X4, on the other hand, is thought to vary intrinsically, likely due to changes in the power-law component. [Heinke et al. \(2005a\)](#) identified a period of high flux in ObsID 2735, between 6.7 and 12.8 hr after the start of the observation. We use 0.5–10 keV X-ray fluxes separately for this interval and the other three ObsIDs in 2002, and paired each value with the overlapping GO 9281 F435W flux to compute quasi-instantaneous X-ray-to-optical flux ratios.

We list the X-ray flux values and resulting X-ray-to-(optical or NUV) flux ratios in Table 2. Estimated systematic errors in the quoted X-ray fluxes are at least 5%, and arise from the use of different energy bands, and from uncertainties in modelling the spectra and the line-of-sight absorption column density N_H . Details of the spectral modelling can be found in [Heinke et al. \(2003a\)](#) and [Heinke et al. \(2005a\)](#).

3.2 Optical and NUV *HST* images

We started the reduction of the GO 9281 WFC data with the images that were flat-fielded and corrected for charge transfer efficiency (CTE) losses by the ACS calibration pipeline (CALACS version 8.2.0). These f1c images still suffer from significant geometric distortion, which we corrected for by subsequent processing with the DrizzlePac software ([Gonzaga et al. 2012](#)). First, the small relative offsets of the f1c images were corrected for with the routine tweakreg. The aligned individual images were then used as input for `astrodrizzle` to create twice-oversampled (to 0.025'' pixel $^{-1}$)

Table 3. Properties of the (likely) optical and NUV counterparts of the 47 Tuc qLMXBs

ID	α_{2000} (h m s)	δ_{2000} (° ′ ″)	d (″)	U_{300}	B_{390}	B_{435}	R_{625}	$H\alpha_{658}$
X4 _{opt}	00:23:53.986	−72:03:50.13	0.06	24.93(3)	24.599(18)	24.20(4)	22.116(15)	21.343(17)
X5 _{opt}	00:24:00.958	−72:04:53.22	0.08	22.997(14)	22.318(9)	21.847(17)	20.334(11)	19.732(15)
X7 _{opt}	00:24:03.501	−72:04:51.96	0.07	23.06(2)	21.74(2)	21.289(17)	19.836(17)	19.42(2)
W17 _{NUV}	00:24:08.307	−72:04:31.44	0.05	22.883(18)	23.17(3)	≥ 24
W37	≥ 21.3	≥ 20.1	≥ 20.1

The columns α_{2000} and δ_{2000} give the coordinates of the (likely) optical/NUV counterpart in the stacked GO 9281 images (X4_{opt}, X5_{opt}, X7_{opt}), or in the stacked GO 12950 images (W17_{NUV}). The column d is the angular offset between the X-ray and optical/NUV positions after applying the boresight correction. The counterparts lie well within the 95% error circle around the boresighted *Chandra* positions ($\sim 0.36''$). Magnitudes were measured from the stacked images, and thus represent averages. Errors on the magnitudes (in parentheses) are formal DAOPHOT 1 σ errors on the last significant digit(s). Systematic errors on the absolute magnitude calibration can amount up to 2% (Sirianni et al. 2005). We have not identified a counterpart to W37 and provide lower limits to its magnitudes.

stacked images in each filter that are corrected for geometric distortion. Three short 10 s exposures, which were taken to obtain photometry of bright cluster stars, were excluded from the stacks. The stacked images are cosmic-ray cleaned with the effects of bad columns and hot pixels removed as much as possible.

We reduced the GO 9019 HRC data in a similar way, starting from the pipeline-processed (CALACS version 9.2.0) flat-fielded images. This program was executed about a month after the installation of ACS on *HST* in 2002 March. The effects of CTE degradation are therefore negligible, and we have not corrected for it. As for the GO 9281 data, the GO 9019 flt frames were aligned with `tweakreg` and stacked with `astrodrizzle` with a factor of two oversampling to produce an image scale of $0.0125'' \text{ pixel}^{-1}$ in the final stacked images.

The starting point for the reduction of the GO 12950 UVIS data was the flat-fielded images from the UVIS pipeline (CALWF3 version 3.1.2). We ran the dedicated STScI software² to correct for CTE losses, before aligning and stacking the images with `DrizzlePac`. The scale of the image stacks is $0.02'' \text{ pixel}^{-1}$. Details can be found in Rivera Sandoval et al. (2015).

3.2.1 Astrometry

The *Chandra* ACIS-S absolute astrometry is tied to the International Celestial Reference System (ICRS) with an accuracy of $\sim 1.1''$ (90% confidence)³. The absolute astrometry of our distortion-corrected *HST* images on the other hand, can be off by $\sim 1''$ or more (Koeke-moer et al. 2005). To make the optical identification of the *Chandra* sources easier, we first tie the *HST* astrometry to the ICRS using UCAC2 stars, which have positional errors $\leq 0.070''$ (Zacharias et al. 2004). However, the few UCAC2 standards in the GO 9281 images are often saturated even in the 10 s exposures. Therefore, we do the astrometric calibration in several steps. First, we astrometrically calibrated a ground-based image of 47 Tuc. From the ESO archive we obtained a 30 s V image taken with the 2.2m/Wide Field Imager (WFI) at La Silla, Chile on 2002 October 29. An astrometric solution was derived based on 225 UCAC2 stars; fitting for relative shift and rotation, pixel scale, and distortions, gives rms residuals of $\sim 0.035''$ in right ascension and in declination. Using 126 stars that are unsaturated and relatively isolated in the WFI and the short GO 9281 F435W exposure, we derived an astrometric solution for

the latter, which has rms residuals of $\sim 0.030''$ in each direction. Finally, this solution was transferred to the stacked GO 9281 images with negligible errors using $>10\,000$ stars. We estimate the final 1σ accuracy of the WFC absolute astrometry as the quadratic sum of the random errors in the UCAC2 positions, the UCAC2–WFI tie and the WFI–*HST* tie, augmented with the estimated systematic error in UCAC2 positions (10 mas, Zacharias et al. 2004). This results in an error of $\sim 0.095''$. We checked for a systematic offset between the *Chandra* and *HST* astrometry by computing the weighted average of the differences in *Chandra* and WFC positions of 29 known matches between X-ray sources and their optical counterparts (see e.g. the finding charts in Edmonds et al. 2003a,b). The resulting offset (X-ray minus optical) is $\Delta\alpha = -0.027'' \pm 0.006''$ and $\Delta\delta = +0.060'' \pm 0.009''$.

The GO 12950 images were calibrated in a similar way, yielding a final error in the astrometry of $0.074''$, and a small boresight correction of $\Delta\alpha = -0.023'' \pm 0.008''$ and $\Delta\delta = -0.003'' \pm 0.009''$.

We apply the boresight correction to the *Chandra* positions and looked for optical and NUV counterparts in the 95% error circles, computed by adding the appropriate errors in the optical (or NUV) positions, the X-ray positions, and the boresight errors (in quadrature). The GO 9019 and HUGS images were not explicitly aligned to the X-ray positions, but it was easy to cross-reference them to the aligned GO 9281 and GO 12950 images by eye.

3.2.2 Photometry

We used the IRAF DAOPHOT package to extract magnitudes from the stacked GO 9281 and GO 12950 images with point spread function photometry. For the GO 12950 images, we also carried out photometry with the KS2 package (Anderson et al. 2008) as an independent check. In general, KS2 and DAOPHOT produce consistent results. Unless mentioned otherwise, we report the DAOPHOT magnitudes in this paper. All photometry is calibrated to the Vega-mag system using the STScI zeropoints. We denote calibrated magnitudes in the F300X, F390W, F435W, F625W, and F658N filters by U_{300} , B_{390} , B_{435} , R_{625} , and $H\alpha_{658}$, respectively. To compute dereddened magnitudes, we converted the cluster reddening of $E(B - V) = 0.04 \pm 0.02$ to filter-specific extinction values. For the NUV filters, we obtained $A(U_{300}) = 0.26 \pm 0.13$ and $A(B_{390}) = 0.18 \pm 0.08$ using the UVIS Exposure Time Calculator. For the optical filters, the conversions given in Table 14 in Sirianni et al. (2005) yield $A(B_{435}) = 0.16 \pm 0.08$, $A(R_{625}) = 0.11 \pm 0.05$, and $A(H\alpha_{658}) = 0.10 \pm 0.05$. Optical and NUV fluxes used to estimate

² http://www.stsci.edu/hst/wfc3/tools/cte_tools

³ <http://cxc.cfa.harvard.edu/cal/ASPECT/celmon/>

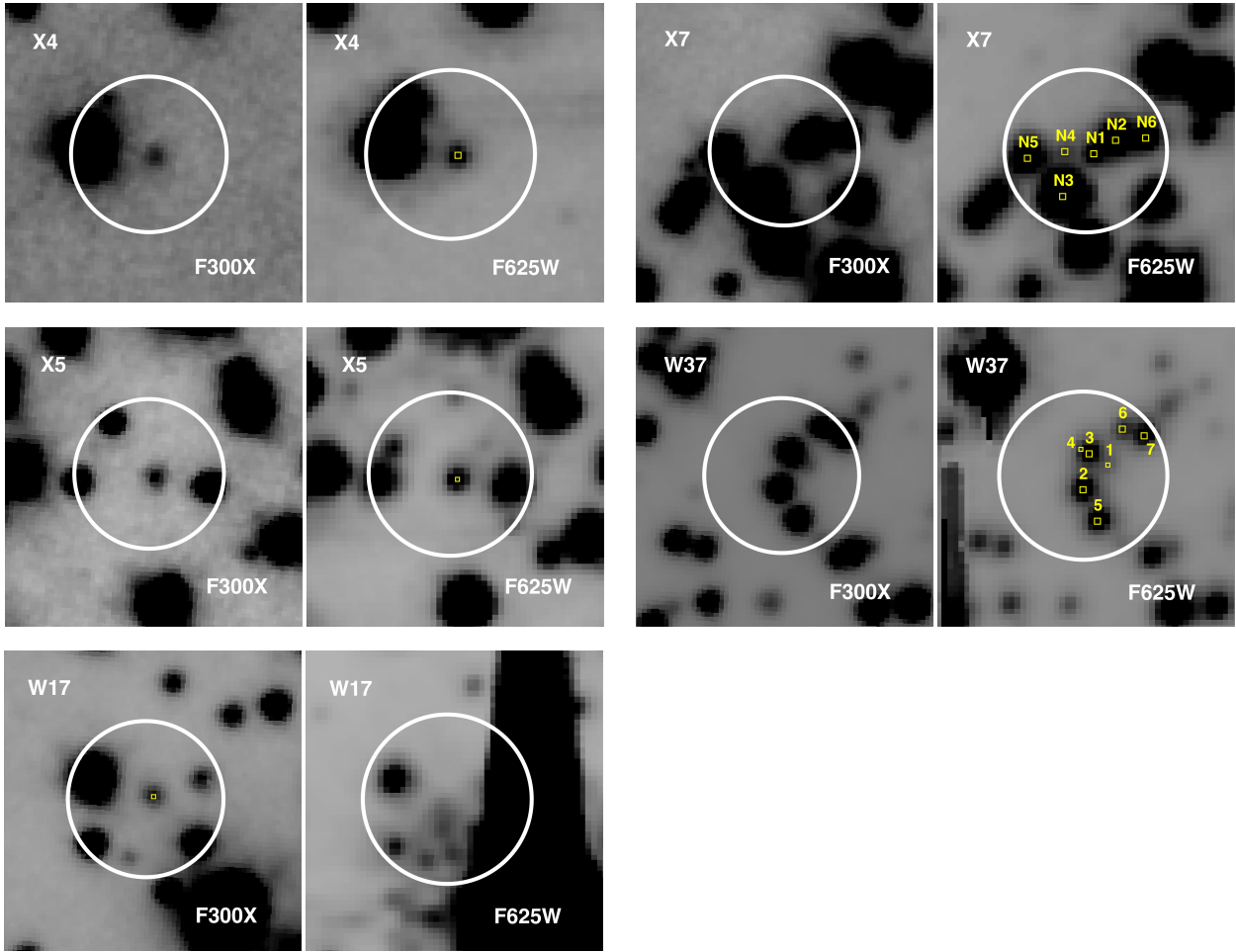


Figure 1. Finding charts for the five qLMXBs discussed in this paper, showing $1.3'' \times 1.3''$ sections from the GO 12950 F300X and GO 9281 F625W stacked images. White circles are the 95% error circles that combine the error in the X-ray position, the absolute astrometry of the *HST* images, and the boresight. The counterparts for X4, X5 and W17 are marked with small unlabelled yellow squares in the image where it is best visible. For X7 and W37, sources that are discussed in the text are labeled. We propose N1 as the counterpart for X7. North is up, east to the left.

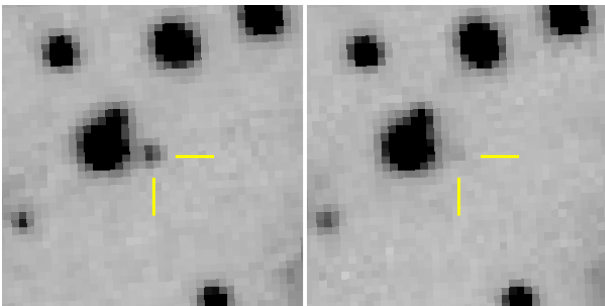


Figure 2. Two GO 9281 F435W images ($2'' \times 2''$) that illustrate the variability of $X4_{\text{opt}}$ (indicated with yellow tick marks). The exposures were taken 2.8 days apart (left: 2002 September 30 3:22 UT, right: 2002 October 2 22:39 UT). At $B_{435} \approx 24.1$, the counterpart is 1.2 mag fainter in the second epoch than in the first epoch. North is up, east is to the left.

puted from the dereddened magnitudes using the zeropoint fluxes provided by STScI.^{4,5}

In order to create optical light curves for the (candidate) counterparts, we ran aperture photometry on the individual images (except for the short exposures). Observation times were converted to barycentric times. We created NUV light curves with the DOLPHOT software (Dolphin 2000). DOLPHOT also produces average photometry, which we find to be in general agreement with the DAOPHOT and KS2 photometry. More details about the photometric analysis can be found in Rivera Sandoval et al. (2015, 2018).

We carried out aperture photometry on the twice-oversampled, drizzled GO 9019 frames using the DAOPHOT FIND and PHOT utilities. We used a 2 pixel radius (0.025 arcsec) aperture and corrected the flux to an infinite aperture using the encircled energy fractions from Table 4 in Sirianni et al. (2005). The magnitudes were calibrated to the Vega-mag system using the zeropoints from Table 11 in

⁴ <https://acszeropoints.stsci.edu>

⁵ <https://www.stsci.edu/hst/instrumentation/wfc3/data-analysis/photometric-calibration/uv-vis-photometric-calibration>

X-ray-to-optical or X-ray-to-NUV flux ratio's (Table 2) were com-

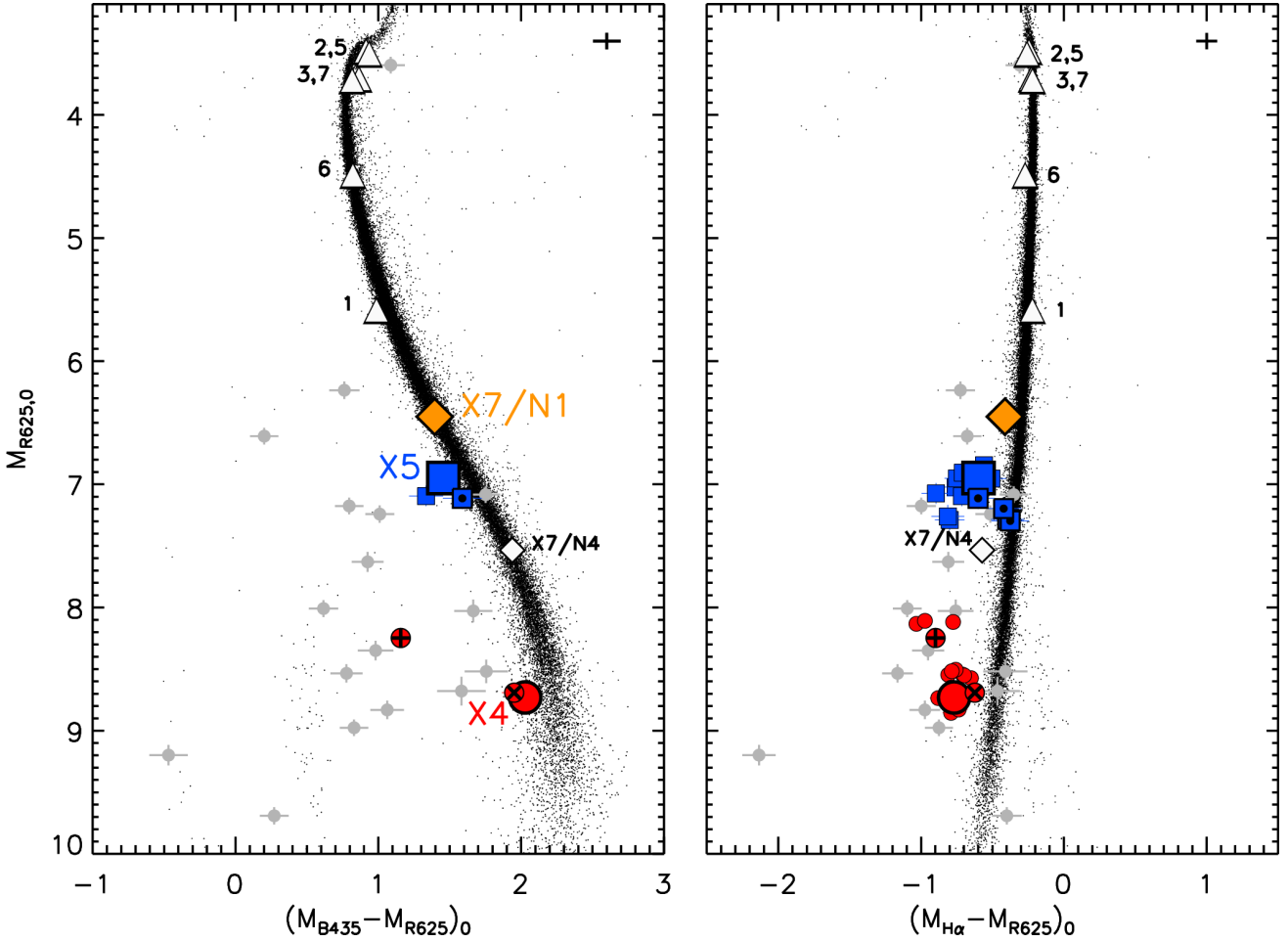


Figure 3. GO 9281 R_{625} versus $B_{435} - R_{625}$ and R_{625} versus $H\alpha_{658} - R_{625}$ colour-magnitude diagrams showing the average photometry of X4_{opt} (large red circle), X5_{opt} (large blue square), and the likely counterpart for X7 (N1, orange diamond). Stars close to the *Chandra* position of W37 (1–3 and 5–7 in Fig. 1; star 4 is only detected in B_{435}) are plotted as upward triangles, N4 near X7 as an open diamond. For X4_{opt} and X5_{opt}, the smaller symbols show the quasi-instantaneous colours. For X4_{opt}, the + (×) signs mark measurements taken when the X-ray flux was high (low); see the light curve in Fig. 6 (bottom) for the corresponding data points. For X5_{opt}, black dots mark colours from visit 2 around the time of X-ray eclipse (see light curves in Figs. 9 and 10). Magnitudes are converted to dereddened absolute magnitudes using a distance $d=4.53$ kpc and reddening $E(B - V)=0.04$. For comparison, colours of securely identified CVs in 47 Tuc are shown as grey circles (Rivera Sandoval et al. 2018). In the top right, we indicate the uncertainty as a result of errors on the reddening and the distance modulus.

Sirianni et al. (2005). In order to filter out outliers, such as blended stars and PSF artifacts, we only included objects in the CMD for which the positions across frames agreed to within 0.7 pixels.

4 RESULTS

4.1 X4

X4 was first detected in ROSAT High Resolution Imager (HRI) observations of 47 Tuc (Hasinger et al. 1994). The source was identified with W125 in the catalog of sources inside the cluster’s half-mass radius detected in the *Chandra* data from 2000 and 2002 (Heinke et al. 2005b). The model for X4’s X-ray spectrum requires a soft component in addition to a dominant harder component to yield an acceptable fit. Consequently, X4 was classified as a likely qLMXB based on its spectral resemblance to other such sources. During the 2002 *Chandra* observations, X4 displayed variability on time scales of $\lesssim 1$ day. As X4 brightened in ObsID 2735, its spectrum became harder, indicating that a reduction in N_H

not responsible for the increase in count rate. Heinke et al. (2005a) argued in favor of changes in the power-law component driving the variability, possibly a sign of ongoing accretion.

X4 lies $\sim 1.4'$ to the north-west of the centre of 47 Tuc, and outside the field of view of the *HST* images analyzed by Edmonds et al. (2003a,b) to look for optical counterparts to *Chandra* sources. Beccari et al. (2014) examined the GO 9281 F658N (but not the F435W and F625W) images that we also analyze here, and reported a likely counterpart with excess $H\alpha$ emission. In order to look for $H\alpha$ -excess sources, they combined the $H\alpha_{658}$ magnitudes from GO 9281 with V (F606W) and I (F814W) magnitudes from ACS/WFC program GO 10775 (also included in HUGS), taken ~ 3.5 yr after the GO 9281 data. As we show below, X4 is considerably variable in the optical as well. As a result, colours constructed from non-contemporaneous measurements can be affected by variability. We revisit X4’s $H\alpha_{658}$ colour below.

In the GO 9281 data, we readily found a variable object at only $0.06''$ from the boresighted *Chandra* position of X4 (Fig. 1, top-left). Comparison of its coordinates with those of the counter-

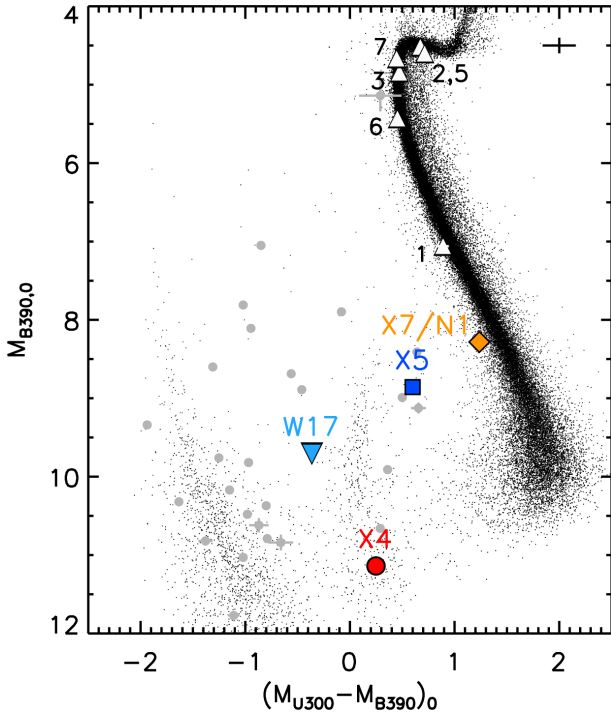


Figure 4. GO 12950 B_{390} versus $U_{300} - B_{390}$ colour-magnitude diagram. The (likely) counterparts to X4, X5, X7 and W17 are plotted with coloured symbols. Photometry is extracted from the stacked images, so variability (see Fig. 8) is “averaged out”. Stars close to the *Chandra* position of W37 are plotted as open upward triangles; star 4 is omitted since its photometry is very uncertain (see text). Magnitudes are converted to dereddened absolute magnitudes using $d=4.53$ kpc and $E(B - V)=0.04$. The uncertainty as a result of errors on the reddening and distance modulus is indicated in the top right. For comparison, colours of securely identified CVs in 47 Tuc are shown as grey circles (Rivera Sandoval et al. 2018).

part found by Beccari et al. (2014) shows that these are the same object. X4 lies in an uncrowded part of the cluster. Examination of the individual GO 9281 exposures, in which X4’s likely counterpart (X4_{opt} henceforth) is easily resolved, reveals that this star is clearly distinguishable in some images but almost fades away in others. In Fig. 2 we compare images from 2002 September 30 and October 2. The counterpart dimmed by $\Delta B_{435} \approx 1.2$ mag in ~ 2.8 days. Its average magnitudes as derived from the stacked images, place it to the blue and $H\alpha$ -bright (i.e. left) side of the bottom of the main sequence in the optical colour-magnitude diagram (CMD) of GO 9281 (Fig. 3; large red filled circle). At increasingly shorter wavelengths, we see that X4_{opt} becomes relatively bluer. In the NUV CMD of GO 12950, the object lies between the 47 Tuc main sequence and the white-dwarf sequence (Fig. 4), a region also occupied by background stars in the Small Magellanic Cloud. The position and optical/NUV magnitudes of X4_{opt} can be found in Table 3.

In the HUGS B_{435} versus $U_{336} - B_{435}$ CMD X4_{opt} lies in a similar region, and for the bluest HUGS CMD, the counterpart falls right on the white-dwarf sequence (Fig. 5, middle and left CMDs). Long-term brightness variations add uncertainty to the blue HUGS colours of X4 since the combined data sets are non-contemporaneous. The relative location of X4_{opt} with respect to the main sequence is qualitatively different in the reddest (I_{814} versus $V_{606} - I_{814}$) CMD, where it lies slightly to the red or above the

main sequence (Fig. 5, right CMD). The HUGS catalogue does not provide a proper-motion membership probability for X4_{opt}.

In order to establish to what extent variability impacts the colours of X4_{opt}, we also examine its quasi-instantaneous GO 9281 colours. We created light curves in the B_{435} , R_{625} and $H\alpha_{658}$ filters using aperture photometry on the individual exposures, adopting a small aperture radius of 1.5 pixels to minimise contamination by the nearby bright star to the east (see Fig. 6, bottom row). By combining pairs of R_{625} and $H\alpha_{658}$ measurements that are closest in time (~ 6 – 7 min apart), we constructed fifteen $H\alpha_{658} - R_{625}$ measurements; these are plotted as small red circles in the right panel of Fig. 3. The two small red circles in the left panel represent $B_{435} - R_{625}$ colours from images taken ~ 19 min apart (the time separation is different here because of the observing sequence). With plus-signs inside the red circles we have marked one $B_{435} - R_{625}$ and one $H\alpha_{658} - R_{625}$ measurement taken during a ~ 31 min time span during the high X-ray flux interval in ObsID 2735 (individual data points are marked in the bottom-left panel of Fig. 6). Similarly, we marked a pair of colours taken during the low X-ray flux interval with x-shaped crosses (see also the bottom-middle panel of Fig. 6). We find that X4_{opt} shows large optical brightness and colour variations that appear to be correlated with its behaviour in X-rays. When the X-ray flux is high, X4_{opt} is brighter, bluer, and has a larger $H\alpha_{658}$ excess than during the remainder of GO 9281 (see middle and bottom rows of Fig. 6). The observed X-ray/optical correlation supports the interpretation that the rise in X-ray emission is caused by a temporary higher accretion rate. The average colour of X4_{opt}, as well as the colours during the high and low X-ray flux intervals, are also plotted in the colour-colour diagram (CCD) of Fig. 7. We infer that the strength of the $H\alpha_{658}$ excess emission in terms of equivalent width (EW) can vary at least between about -30 Å and -80 Å. The average EW in the GO 9281 images is about -50 Å, larger than the EW estimate by Beccari et al. (2014) of -28 Å.

In the GO 12950 images, the object is significantly variable in U_{300} as well, by ~ 1.6 mag (although at the faint end magnitude errors are ~ 0.4 mag). In B_{390} , the source is more stable (Fig. 8).

4.2 X5

The *Chandra* light curve of X5 (or W58) shows eclipses at an ~ 8.7 hr period as well as “dipping” activity due to rapid changes in the column density obscuring the regions close to the neutron star (Heinke et al. 2003a; see top panel of Fig. 9). These changes are likely caused by inhomogeneities in the outer parts of an accretion disk seen (almost) edge on. Using the precise *Chandra* position, Edmonds et al. (2002a) identified the counterpart (X5_{opt}) as a blue object in WFPC2 images that shows variability on long and short time scales (see Fig. 1 in Edmonds et al. 2002a and our Fig. 1 for a finding chart). In U (F300W), the short-term variations resemble eclipses and ellipsoidal variations; no such variability was seen by Edmonds et al. in V (F555W). The average U magnitude was found to change by ~ 1 mag between epochs separated by years. While the dipping in X-rays, long-term U variability, and blue $U - V$ colour point to the presence of an accretion disk, Heinke et al. (2003a) (and later Bogdanov et al. 2016, with even more stringent constraints) found that any contribution from non-thermal emission to the *Chandra* spectrum is negligible. As suggested by Heinke et al. (2003a), gas from the disk may not currently be reaching the neutron star. Possibly, gas is building up in the disk, or it could be swept away by a pulsar wind or propeller effect before arriving at the neutron-star surface.

In the GO 9281 photometry, X5_{opt} is also blue (although not

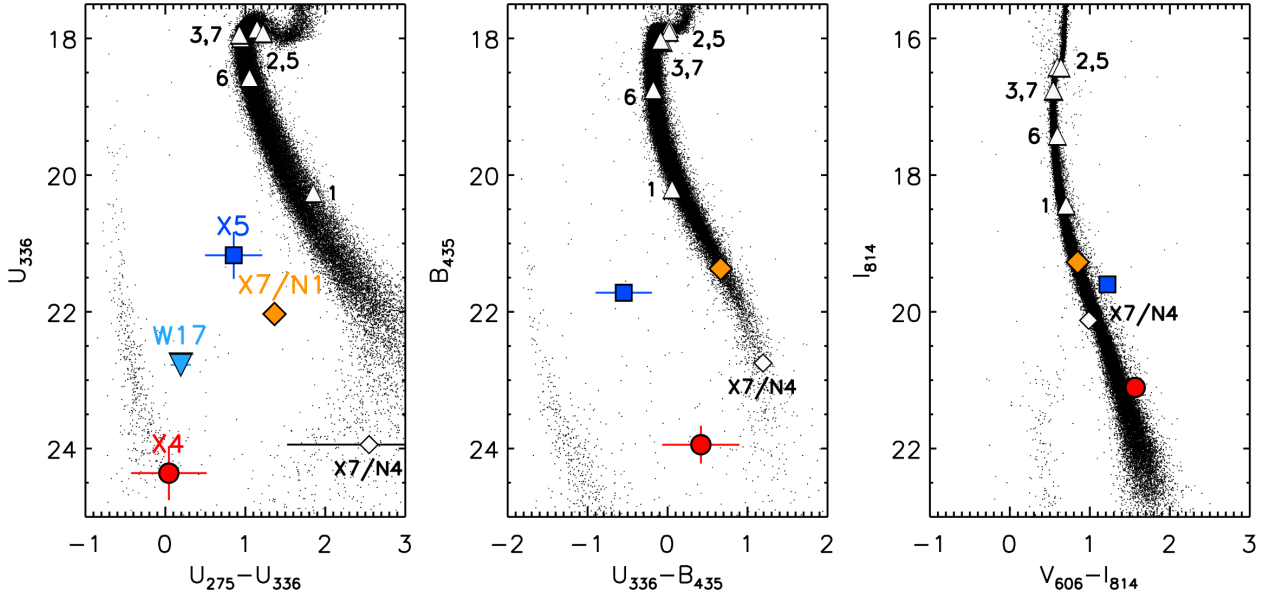


Figure 5. HUGS colour-magnitude diagrams with the (likely) counterparts marked with coloured symbols. The HUGS photometry in F275W, F336W and F435W is not contemporaneous (see Table 1), which could affect the blue colours of objects in the HUGS catalogue if they are (long-term) variables. Unlikely counterparts near X7 and W37 are marked with the same (open) symbols as in Fig. 3. Errors on the photometry of the (proposed or unlikely) counterparts are computed with the HUGS-reported rms values divided by square-root of the number of measurements. Error bars are plotted but in some case they are smaller than the symbol sizes. The relatively large (for its brightness) errors of $X5_{\text{opt}}$ in the left and middle panels are dominated by the large rms in the F336W magnitudes.

as pronounced as in $U - V$ and shows $H\alpha$ excess emission (Fig. 3). The simultaneous X-ray and optical light curves of $X5_{\text{opt}}$ show correlated variability in all three filters, in the sense that the optical brightness also decreases around the time of the X-ray eclipses (Fig. 9, middle and bottom rows). This is illustrated more clearly in the folded light curves of Fig. 10, where we adopted an orbital period of 31200.197(1) s (see Appendix A). The folded X-ray light curve in the top panel of Fig. 10 only shows those time intervals that are simultaneous with the optical data (middle). Double maxima and minima per orbital phase are seen most clearly in the R_{625} light curve. These features could be the combined effect of ellipsoidal variations and eclipses, or a signature of multiple shocks that give rise to hot spots in the disk (see e.g. Kononov et al. 2017 for the cataclysmic variable V455 And in quiescence, and D’Avanzo et al. 2005 for the neutron-star LMXB Cen X-4 in quiescence). Moreover, as the hot disk should be more extended than the region from which the X-rays originate, the optical/NUV eclipse should also last longer. This likely explains why the optical minimum around phase 0 is broader than the X-ray eclipses, as was also noted by Edmonds et al. (2002a) for the U band. Parts of the hot disk could be obscured by the stream impact point, as well, which would shift the midpoint of the optical/NUV eclipse to earlier phases. The sampling of our light curve is not good enough to see this potential effect.

The quasi-instantaneous colours, computed in the same way as for $X4_{\text{opt}}$, show that $X5_{\text{opt}}$ moves closer to the main sequence in $H\alpha_{658} - R_{625}$ around phase 0 (defined to be the centre of the X-ray eclipse; Fig. 3). In the bottom-middle panel of Fig. 9, the data points that were combined to compute the colours around the X-ray eclipse are marked with filled dots, which makes them easier to recognise in the folded light curve of Fig. 10, the CMD of Fig. 3, and the CCD of Fig. 7. Towards the end of this optical dip, around 3.25 days after the start of GO 9281, the $H\alpha_{658} - R_{625}$ excess is again at the average level for $X5_{\text{opt}}$ (see the left-most “dotted” blue square in the R_{625} versus $H\alpha_{658} - R_{625}$ CMD in Fig. 3). The $B_{435} - R_{625}$

colour at this time also lies closer to the main sequence compared to the average, but the corresponding individual B_{435} and R_{625} data points lie in a part of the light curve where the brightness may be changing relatively quickly, which could affect the colour. These changes suggest that part of the region where the $H\alpha$ (and perhaps also blue) emission is relatively strong, is obscured together with the X-rays. Unlike Edmonds et al. (2002a), who noted that $X5_{\text{opt}}$ shows no signs of eclipses or ellipsoidal variability in V , we do see variations at the redder wavelengths. This suggests long-term qualitative changes in the light curve. The minima around phase 0.5 in R_{625} and $H\alpha_{658}$ could be ellipsoidal variations. On the other hand, there is no obvious dip around that phase in B_{435} ; given the poor sampling, we cannot draw firm conclusions. The light curve looks especially noisy around phases 0.2–0.4 in $H\alpha_{658}$ (Fig. 10). This interval overlaps with the part of the X-ray light curve most affected by dipping.

In the GO 12950 data, the counterpart to X5 is much bluer relative to the main sequence than in the optical (Fig. 4). With $U_{300} \approx 22.3$ at maximum brightness, the source is about as bright as in 1997 November and 1999 October, but almost a magnitude fainter than in 1995 October (Edmonds et al. 2002a). The uncertainty in the orbital period is small enough that we can phase-connect the X-ray/optical light curves from 2002 with the NUV light curve from GO 12950 taken about 11 years later (see Appendix A). In the bottom panel of Fig. 10, we show the phased NUV light curve taken over a time span of ~ 6.5 hr. The U_{300} light curve looks smooth, and shows a broad dip centred around the X-ray eclipse. The four B_{390} data points show a lack of variability. Unfortunately, in the other four F390W exposures, X5 falls in a chip gap.

In the HUGS CMDs, $X5_{\text{opt}}$ is blue except in the reddest filters, where it lies ~ 0.35 mag to the red of the main sequence in $V_{606} - I_{814}$. This excess may be explained by periodic changes in the light curve on a time scale of hours affecting the colours, or intrinsically anomalous colours of the donor.

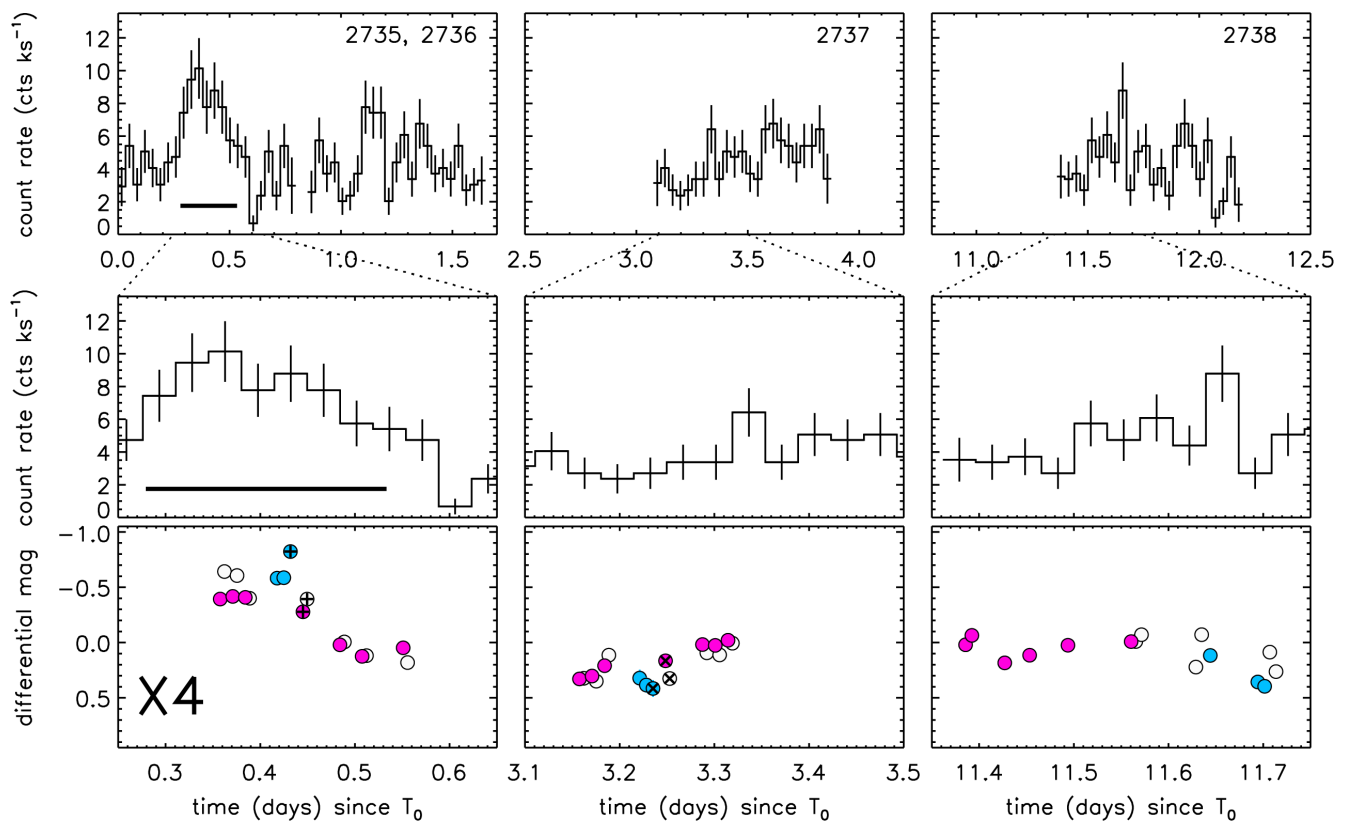


Figure 6. Simultaneous *Chandra* and GO 9281 light curves of X4. The top row shows the X-ray light curves (0.3–8 keV) from the four long 2002 *Chandra* observations (labeled by ObsID). The middle row zooms in on the sections with simultaneous *HST* coverage. The thick horizontal lines in the top-left and middle-left panels indicate the high X-ray flux interval between 6.7 hr and 12.8 hr after the start of the observation. In the bottom panel we show the optical light curves (F435W: blue; F625W: pink; F658N: white) after subtracting the average magnitudes. The three circles with + signs (bottom-left) mark the B_{435} , R_{625} and $H\alpha_{658}$ magnitudes that were combined to compute colours when the X-ray flux is high, and the three circles with × signs (bottom-middle) mark magnitudes that were combined to compute colours during the low X-ray-flux interval. Time on the x-axis is in units of days since the start of the first 2002 *Chandra* observation (2002 Sep 29 17:01 UTC).

4.3 X7

X7 (or W46) is one of the best-studied X-ray sources in 47 Tuc. A neutron-star atmosphere model gives an excellent fit to the *Chandra* spectrum. The lack of a harder power-law spectral component, and the high level of stability in X-rays over the years, suggest there is no accretion occurring in the system. This makes X7 an attractive source for deriving constraints on the neutron-star equation of state (Heinke et al. 2006; Bogdanov et al. 2016). Some systematic uncertainties in X7’s radius and mass measurements remain, because the composition of the neutron-star atmosphere is unknown. Although an H-rich atmosphere is deemed more likely than a He-rich atmosphere (see the discussion in Bogdanov et al. (2016) and Steiner et al. (2018)), the nature of the optical or NUV counterpart would shed more light on this issue. However, no counterpart has been identified yet. Edmonds et al. (2002a) found no variable or blue source in the X-ray error circle.

We examined the colours of the three nearby stars that were also considered by Edmonds et al. (2002a), N1 to N3 (see Fig. 1 top right for a finding chart). Like these authors, we find that N2 and N3 have normal main-sequence colours in the GO 9281 and GO 12950 images, so we agree that these stars are not viable counterparts; moreover, their angular separations from X7’s *Chandra* position are relatively large. At an offset of $\sim 0.07''$, N1 is an excellent astrometric match to X7. However, its $U - V$ colour resembles that of a normal low-mass main-sequence star, and in the high-

cadence GO 8267 WFPC2 time series spanning 8.3 days N1 shows no variability (see Fig. 3d in Edmonds et al. 2002a). We find that the $B_{435} - R_{625}$ colour of N1 is also unremarkable, and consistent with that of a $\sim 0.62 M_{\odot}$ main-sequence star (based on comparison with the isochrones from Bressan et al. 2012). On the other hand, its $H\alpha_{658} - R_{625}$ colour puts it slightly to the H α -excess side of the main sequence (see Fig. 3). Interestingly, in the B_{390} versus $U_{300} - B_{390}$ CMD, N1 lies a little bit to the blue of the main sequence (Fig. 4). This modest blue excess is also found independently in the KS2 photometry of the same data, where the apparent deviation from the main sequence is in fact a bit larger. (Below, we quantify N1’s blue excess in more detail for the GO 9019 CMDs, where it is found in a similar location with respect to the main sequence). Its U_{300} light curve (Fig. 8, top) shows scatter at a level that is higher than $\geq 99\%$ of stars with a similar magnitude (Fig. 11). We also identify a faint star at an offset of $\sim 0.15''$ from X7 that is visible (but unnamed) in the V finding chart in Edmonds et al. (2002a), as well. We name this star N4 and mark it in the finding chart of Fig. 1. N4 has a small H α excess that is more pronounced than that of N1, but lies on the main sequence in the $B_{435} - R_{625}$ CMD. From the NUV images, we find that $B_{390} = 24.18(4)$ but since this star is undetected in U_{300} , we do not know its NUV colour. However, the limit on U_{300} suggests that $U_{300} - B_{390} \geq 1.8$. There are two more stars inside the error circle (N5 and N6); both lie on the main sequence, and therefore we do

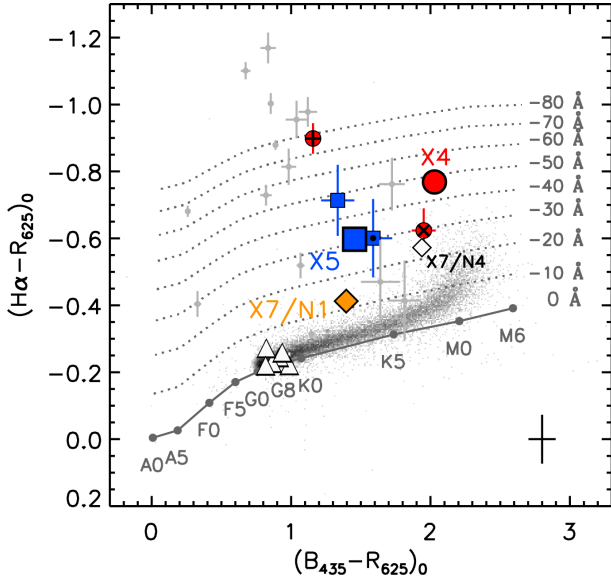


Figure 7. GO 9281 colour-colour diagram with the average colours of the (likely) counterparts marked with the larger coloured symbols. The small symbols show the quasi-instantaneous colours for $X4_{\text{opt}}$ and $X5_{\text{opt}}$. Unlikely counterparts near X7 and W37 are marked with the same (open) symbols as in Fig. 3. The photometry has been dereddened using $E(B - V) = 0.04 \pm 0.02$. The grey solid line connects the synthetic colours of stars as computed from Castelli-Kurucz model spectra of $\log Z = -2.5$ with the Synphot package. The dotted grey lines represent synthetic colours that result from adding a Gaussian emission line with FWHM 25 \AA to the model spectra, with the line strength increasing in increments of $\Delta E W(H\alpha) = -10 \text{ \AA}$. The grey circles are the colours of securely identified CVs in 47 Tuc. In the bottom right, we show the uncertainty as a result of the error on the reddening.

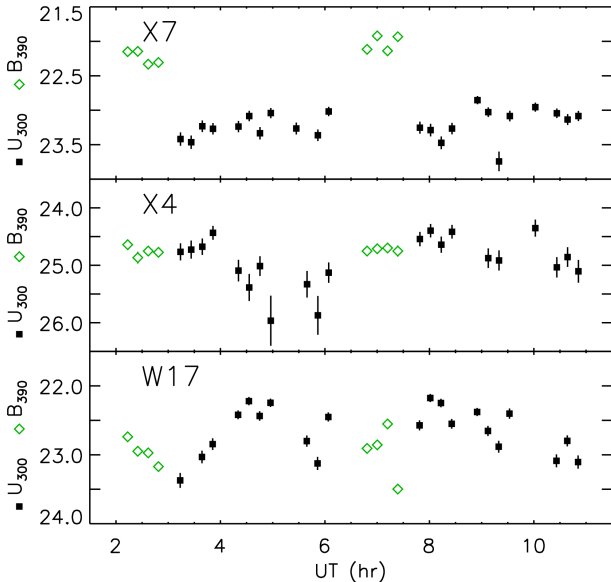


Figure 8. GO 12950 light curves in U_{300} (filled squares) and B_{390} (open green diamonds) for the counterparts to X7, X4 and W17. Magnitudes that could be affected by CRs are excluded. Time on the x-axis is UT on 2013 August 13.

not consider them plausible counterparts. These findings spurred us to focus on N1 and N4, and look for coverage in other *HST* images.

In Fig. 5, we mark N1 and N4 in the HUGS CMD with the orange and white diamond, respectively. N1 lies well to the blue of the main sequence in the U_{275} versus $U_{275} - U_{336}$ CMD, whereas the location of N4 is poorly constrained due to the large errors in U_{275} . In the redder CMDs, both stars lie on, or close to, the main sequence. Taking the HUGS colours at face value, we conclude that N1 is the more likely counterpart given its blue NUV colour and smaller offset from X7. We caution that the value of the “sharp” parameter, which indicates how well a star’s profile matches that of the PSF, is outside the optimal range in all HUGS measurements of N1 and N4. This may be due to the crowding near X7 and could indicate that their photometry is affected.

We examined N1 and N4 in the GO 9019 HRC data as well. N4 is not detected in the GO 9019 F220W and F330W images, only in the F435W and F475W images. N1 is too faint to be detected in F220W. The average $U_{330} - B_{435}$ and $U_{330} - B_{475}$ colours put N1 to the blue of the main sequence. To quantify this blue offset, we first computed the width of the main sequence at the magnitude of N1 in the CMDs of Fig. 12. The solid red lines in the panels represent the mean colour as a function of magnitude, while the dashed red lines are the 1σ deviations about the mean, calculated using an iterated 3σ clip. The curves were smoothed by fitting third-order polynomials. We took half the separation between the dashed lines as the 1σ uncertainty on the colour index, which for N1 is plotted as the error bar on the orange diamond in each panel. N1 lies more than 1σ to the blue side of the main sequence in both CMDs, especially in the $U_{330} - B_{435}$ CMD, suggesting a blue (NUV) excess.

We also considered indications for variability in the individual GO 9019 images. For B_{435} and B_{475} , the DAOPHOT errors are $\sim 0.08 - 0.1$ mag, consistent with the scatter in the magnitudes from the individual images (three in each filter). In U_{330} , N1 shows a 0.35 mag variation between the three images. Going from the first to the third exposure, N1 varies from 21.71(25) mag, to 21.36(18) mag (4 min later) and finally to 21.57(20) mag (19 min after the first image). For all three filters, we compared the standard deviation in the N1 data points with those of other stars in the images, and found that N1 does not stand out. We conclude that N1 is not significantly variable in the GO 9019 images that we analyzed. Comparison between the HUGS magnitude for N1 in F336W from 2010 Sep ($U_{336} = 22.03(07)$) with the value reported by Edmonds et al. (2002a) from 1999 Jul ($U_{336} = 21.97$ with an absolute error ~ 0.2 mag) also shows good agreement.

In conclusion, we consider it very likely that N1 is the true optical/NUV counterpart of X7. The variability in F300X (Fig. 11), the blue colours in the NUV filters and the weak $H\alpha$ excess emission suggest the presence of an accretion disk. However, in X-rays X7 has not shown any signs of ongoing accretion. Possibly, accretion from the secondary feeds the disk but either the gas has not reached the neutron star just yet, or is expelled from the system by a pulsar or propeller wind. Alternatively, low-level accretion is taking place and generates faint X-ray emission of the order $\sim 10^{31} \text{ erg s}^{-1}$, but the corresponding weak power-law component in the X-ray spectrum remains hidden under the $\sim 10^{33} \text{ erg s}^{-1}$ soft X-ray emission. Another implication of N1 being the counterpart, is that the atmosphere of the neutron star in X7 would be H-rich as N1 looks like a main-sequence star with a small $H\alpha$ excess. This is consistent with the conclusions of Bogdanov et al. (2016) and Steiner et al. (2018) from X-ray spectral fitting.

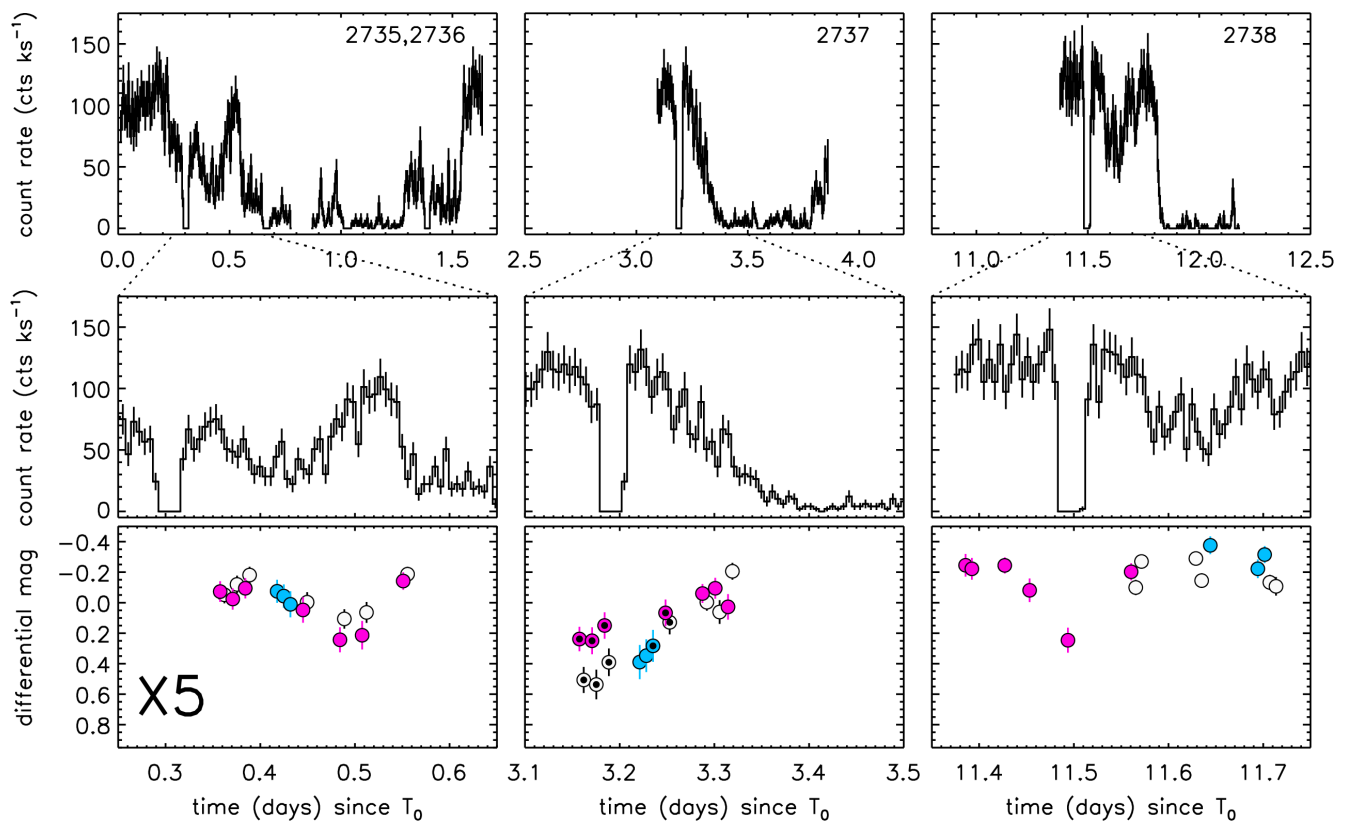


Figure 9. Simultaneous *Chandra* and GO 9281 light curves of X5. The top row shows the X-ray light curves (0.3–8 keV) from the four long 2002 *Chandra* observations (labeled by ObsID). The middle row zooms in on the sections with simultaneous *HST* coverage. In the bottom panel we show the optical light curves (F435W: blue; F625W: pink; F658N: white) after subtracting the average magnitudes. Data points with the black filled dots (in bottom-middle panel) are the magnitudes that were combined to compute the colours of X5 around the time of the X-ray eclipse. Time on the x-axis is in units of days since the start of the first 2002 *Chandra* observation (2002 Sep 29 17:01 UTC).

4.4 W17

W17 is among the new sources that were discovered in the *Chandra* observations of 2000. Edmonds et al. (2003b) identified this source as a candidate qLMXB based on its relatively soft X-ray colours, and the high X-ray-to-optical flux ratio (≥ 0.9) that is inferred from its X-ray luminosity ($L_X \approx 2 \times 10^{31} \text{ erg s}^{-1}$ (0.5–6 keV) for the distance adopted here) and the high upper limit to the optical magnitude ($U \geq 24$). The proximity of a very bright, saturated star at only $\sim 0.62''$ to the south-west hampered their search for an optical counterpart in the deep GO 8267 WFPC2 *V* and *I* data. Fits to the 2000 and 2002 *Chandra* spectra led Heinke et al. (2005a) to the conclusion that W17 is indeed a qLMXB: its spectrum is dominated by a $\Gamma \approx 1.9$ power-law component, but also shows a distinct soft component that can be fitted with a neutron-star atmosphere model. W17 does not show X-ray variability on short time scales (days to weeks) or between the 2000 and 2002 observations.

In our GO 9281 data, the light of the nearby bright star also inhibits a sensitive search for a counterpart, so we have no simultaneous X-ray/optical measurements of this source. We estimate an upper limit of $B_{435} \geq 24$, with an uncertainty of ~ 0.5 mag given that the light of the saturated star makes it difficult to account for the local background. The situation is much better in the NUV. In the GO 12950 images we readily found a very blue star near the centre of the *Chandra* error circle (see Fig. 1). This star is highly variable with a full amplitude of $\Delta U_{300} \geq 1$ mag in the ~ 8 hr time span of the GO 12950 observations (Fig. 8). Its time-averaged

$U_{300} - B_{390}$ colour puts it far to the blue of the main sequence, in between the white dwarfs and the SMC sequence (Fig. 4). The HUGS $U_{275} - B_{336}$ colour puts it even closer to the white-dwarf sequence. In the F435W, F606W, F814W filters, we do not consider the photometry reliable given the proximity of the bright star.

The GO 12950 NUV colours of the counterpart are bluer than those of $X4_{\text{opt}}$ and $X5_{\text{opt}}$. A larger contribution from an accretion disk could be the reason for this. However, the X-ray luminosity of the power-law component in W17 is about the same as the average power-law luminosity in X4, suggesting that on average the level of accretion in these two systems is similar. The orbital period would shed light on the nature of the companion. The shape of the GO 12950 light curves show a hint of repetition at a time scale of ~ 3.5 –4 hr but do not display significant periodicity. If the secondary is a white dwarf rather than a main-sequence star, it could contribute to the blue colours as well.

4.5 W37

W37 is also one of the sources discovered in the 2000 *Chandra* observation. Its spectrum is soft and can be fitted with a neutron-star atmosphere model. W37's X-ray light curve shows eclipses (at a period of 3.087 hr) as well as drastic changes in the count rate due to variable obscuration. During the eclipses, a small amount of residual soft emission of unknown origin was seen by Heinke et al. (2005a). W37 has no known optical or NUV counterpart. No nearby blue or variable object is seen in the *HST* data analyzed by Edmonds

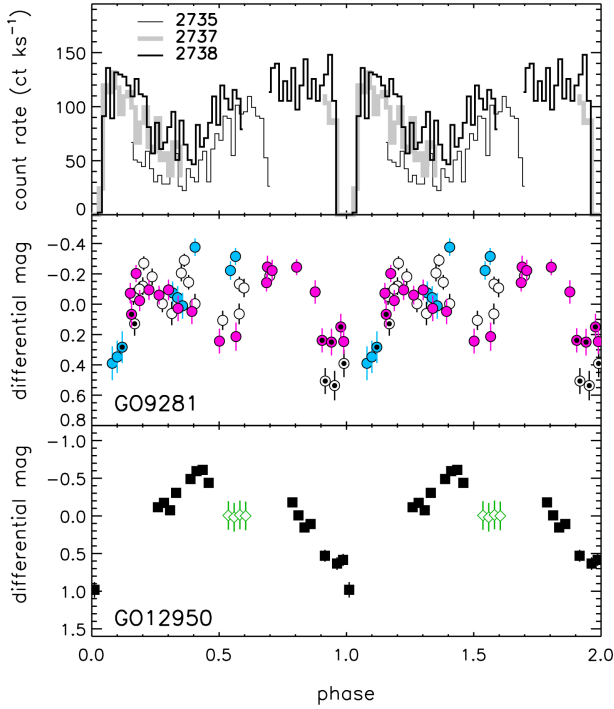


Figure 10. *Chandra* and *HST* light curves for X5, folded on the orbital period of 8.667 hr; phasing was chosen such that the middle of the X-ray eclipse is phase=0. *Top*: The 0.3–8 keV light curves only show the sections that were simultaneous with the GO9281 observations. The line thickness is different for each epoch. *Middle*: GO9281 F435W (blue), F625W (pink), and F658N (white) differential light curves. Black dots mark the data points from visit 2 that were combined to create colours around the time of X-ray eclipse. *Bottom*: GO12950 lightcurves in F300X (filled squares), F390W (open green diamonds).

et al. (2003a), although the presence of two bright main-sequence stars close to the X-ray position reduces the sensitivity to finding faint counterparts. If the companion is a main-sequence star, the orbital period indicates a secondary mass of $\lesssim 0.34 M_{\odot}$.

In the GO9281 and GO12950 images we find seven optical/NUV sources inside the 95% error circle, marked 1 to 7 in the panel for W37 in Fig. 1. Five of these (2, 3, 5–7) look like regular main-sequence or main-sequence turnoff stars, with some lying slightly offset to the red side of the main sequence in $B_{435} - R_{625}$. We do not consider these stars plausible counterparts. Star 1 lies close to the main sequence in the R_{625} versus $H\alpha_{658} - R_{625}$ CMD (near the expected location of a $\sim 0.7 M_{\odot}$ star) and the U_{336} versus $U_{275} - U_{336}$ and I_{814} versus $V_{606} - I_{814}$ CMDs, but in the R_{625} versus $B_{435} - R_{625}$, B_{390} versus $U_{300} - B_{390}$, and B_{435} versus $U_{336} - B_{435}$ CMDs of Figs. 3, 4 and 5, respectively, it appears to be slightly offset to the blue. Given the estimated upper mass limit of a main-sequence donor (see previous paragraph), it is not likely that star 1 is the true counterpart. It could be blended with an undetected fainter and bluer object that draws its photometry to the blue side of the main sequence, or the PSF wings of the nearby star 3 may not be properly accounted for. The photometry for star 4 is ambiguous. In the optical, it is only convincingly detected in the F435W images, at $B_{435} \approx 20.1$. Forcing DAOPHOT to extract R_{625} and $H\alpha_{658}$ magnitudes from the position of this F435W detection, does not produce credible results. In the NUV, the photometry of star 4 puts it either to the red (DAOPHOT) or the blue (KS2, Dolphot) of the main sequence. Given the uncertain photometry, we have omitted

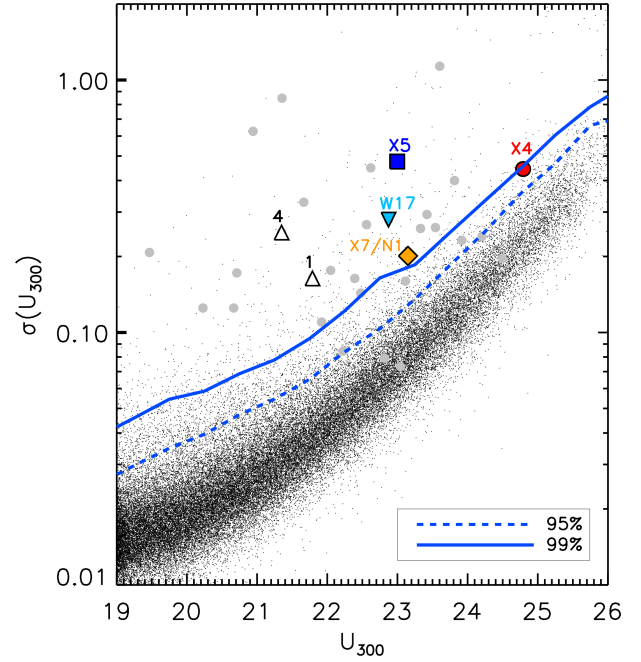


Figure 11. Rms variability in the GO 12950 U_{300} light curves versus average U_{300} magnitude. Outliers were filtered using a 3σ -clipping algorithm. (Likely) counterparts and two stars near the *Chandra* position of W37 are marked with the same symbols as in Fig. 4. For comparison, securely identified CVs from (Rivera Sandoval et al. 2018) are shown as grey filled circles; the CV W36 lies outside the plot ranges, and the CV W23 is omitted as it overlaps with X5_{opt}. The blue dashed lines represent the 95% and 99% limits of the percentile distribution (computed in bins with a 0.5 mag width) below which 95% and 99%, respectively of the stars are found. Other stars in the cluster are represented with black dots.

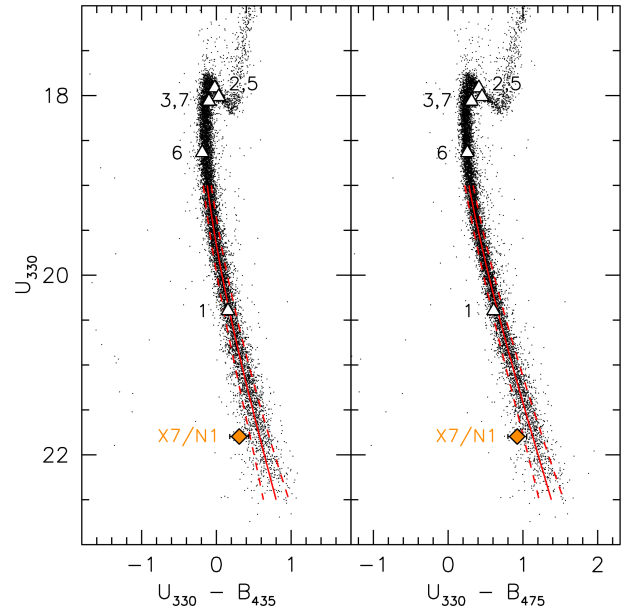


Figure 12. GO 9019 U_{330} versus $U_{330} - B_{435}$ and U_{330} versus $U_{330} - B_{475}$ colour-magnitude diagrams with the likely counterpart to X7 (N1) indicated with an orange diamond. Upward triangles are stars close the *Chandra* position of W37. Solid red lines represent the mean colour as function of magnitude, while the dashed red lines are the 1σ deviations about the mean, calculated using an iterated 3σ clip.

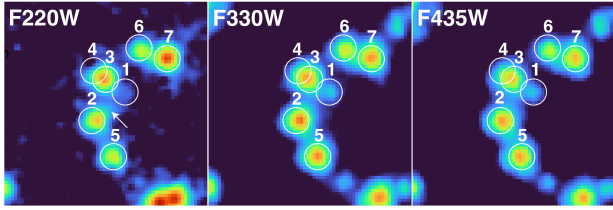


Figure 13. Three-panel GO 9019 ACS HRC finding charts for a $0.8'' \times 0.8''$ region centred on the position of W37. North is up and east is to the left. The excess flux to the north-west of star 2 in the F220 image is indicated with a white arrow. The frames for each filter have been drizzle-combined with $2 \times$ oversampling and are rectified to the *Gaia* reference frame. The drizzled pixel size is $0.0125''$ on a side. The stars are labelled as in the W37 panel of Fig. 1.

this star from Fig. 4. Perhaps the only thing that can be concluded is that, at the time of the GO 9281 observations, this object was blue for it to be detected in the F435W, but not in the F625W and F658N images. Stars 1 and 4 are highly variable in the U_{300} images of the GO 12950 data set; both lie above the 99% percentile limit in Fig. 11. Star 1 was clearly detected in the NUV photometry and the variability seems to be intrinsic, while star 4 seems to be closer to star 3 and variability could be due to contamination from that star. In the HUGS catalog and the GO 9019 images, star 4 is not detected.

Examination of the GO 9019 F220W image suggests the presence of excess flux at a position about $0.06''$ to the north-west of star 2 and about $0.04''$ from the location of W37. This excess flux is not apparent at longer wavelengths, which is consistent with the presence of a blue star. This is illustrated in Fig. 13, which shows the region around W37 in the F220W, F330W, and F435W filters. These drizzled ACS HRC frames have been aligned with the HUGS coordinate system, which itself is aligned with the *Gaia* reference system. While the extension of the image of star 2 in F220W is suggestive of the presence of a blue star near the position of W37, it is by no means definitive. Deeper high-resolution imaging is necessary to further investigate this issue.

In order to identify the counterpart of W37 through optical variability on the known orbital period, we have performed a series of light curve analyses on the GO 8267 WFPC2 data. The F555W and F814W light curves of the four stars closest to the centre of the X-ray error circle (stars 1 to 4) were kindly provided to us by R. Gilliland. The light curves contain 636 (F555W) and 653 (F814W) data points spread over 8.3 days in 1999 Jul. We refer to Gilliland et al. (2000) and Albrow et al. (2001) for more details about the data and light curve extraction. First, we phase-folded the V_{555} and I_{814} light curves on the known period from the X-ray eclipses, but no periodicity was observed in either of the two bands. To reduce the scatter in these light curves, we averaged the measurements in phase bins of 0.001 and 0.003 days, well below the duration of the X-ray eclipse. Still, no periodicity was observed for any of the four stars. Another attempt was carried out by using a sigma-clipping approach on each of the previously defined phase bins. We removed all photometric measurements that were smaller or larger than $m \pm 3\sigma$, where m is the median value in each bin and σ is the standard deviation. This approach was taken to remove outliers, but did not reveal any periodicity. Finally, we performed a Lomb-Scargle (Lomb 1976; Scargle 1982) analysis to look for the X-ray period in the optical data. The analysis was performed separately in both filters. In multiple cases a period corresponding to the *HST* orbit was observed (~ 96.5 min, so very close to half

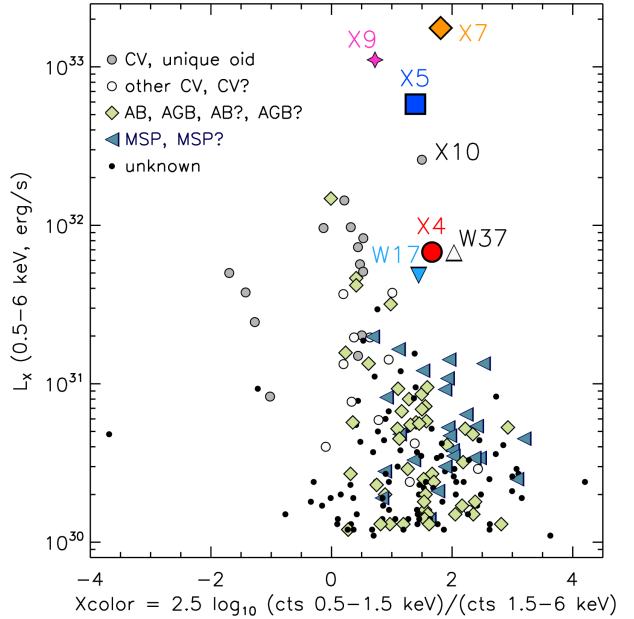


Figure 14. X-ray luminosity versus $(0.5\text{--}1.5\text{ keV})/(1.5\text{--}6\text{ keV})$ X-ray colour for 47 Tuc sources in the 2002 *Chandra* observations (Heinke et al. 2005b). Only sources with more than 20 counts (0.5–6 keV) are included. The qLMXBs and the CV X10 are labelled. Other source classes are plotted with symbols according to the legend in the top left. Classifications were taken from Heinke et al. (2005b) unless the classification was revised by more recent studies. We distinguish between the securely identified CVs with unique optical counterparts (Rivera Sandoval et al. 2018, filled grey circles) and other CVs and CV candidates (open circles).

W37’s orbital period, or 92.6 min), but none consistent with the X-ray period of W37 or half of it.

In conclusion, we have not securely identified the counterpart to W37. To compute limits on the X-ray-to-optical flux ratio (see Table 2) we use the magnitudes of star 4, which is the faintest of the stars near W37.

5 DISCUSSION

Our search for optical/NUV counterparts to the qLMXBs in 47 Tuc has yielded the discovery of a blue and variable counterpart to W17. We also find compelling indications that a known astrometric match to X7 is indeed a likely counterpart. Of the five (likely) neutron-star qLMXBs in the cluster, only one (W37) remains unidentified as the proximity of several stars near the centre of the X-ray error circle complicates a sensitive search for a counterpart. Optical counterparts have been identified for only two other globular-cluster qLMXBs⁶: the source in ω Cen (discovered by Haggard et al. (2004), later named 44e by Haggard et al. (2009)) and U24 in NGC 6397 (Heinke et al. 2014). With $R_{625}=25.2$ and $R_{625}=26.2$, respectively, these systems are much fainter than the 47 Tuc qLMXBs (with R_{625} between 19.8 and 22.1, see Table 3), making them unsuitable for detailed follow-up studies. The ω Cen and NGC 6397 systems are also intrinsically much fainter in the optical ($M_{625}=11.6$

⁶ and for a handful of globular-cluster transient LMXBs in quiescence, including IGR J18245–2452 in M 28 (Pallanca et al. 2013); Terzan 5 X-1 and Terzan 5 X-2 (Ferraro et al. 2015; Testa et al. 2012); and SAX J1748.9–2021 in NGC 6440 (Verbunt et al. 2000; in’t Zand et al. 2001)

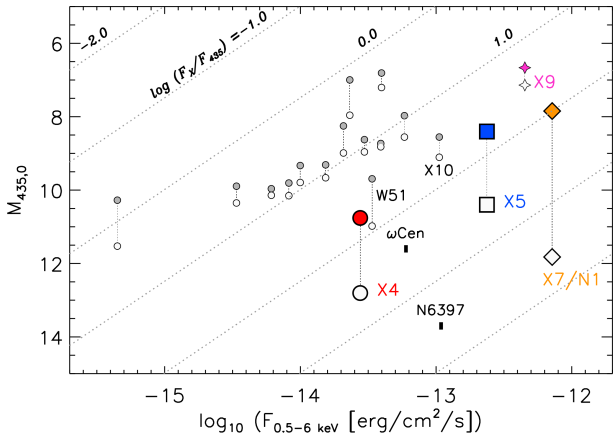


Figure 15. Filled symbols show the absolute B_{435} magnitudes of the qLMXBs (coloured) and CVs (grey) versus the X-ray fluxes (0.5–6 keV, from Table 2 in Heinke et al. (2005b)) from the simultaneous 2002 *HST* and *Chandra* data. Open circles mark the lower limit on the excess blue fluxes (see text). The vertical dotted lines mark the range where the actual contribution from the accretion flow to the blue light is expected. The diagonal dotted lines mark lines of constant X-ray to B_{435} flux ratio. For comparison, we also show the two other globular-cluster qLMXBs with optical counterparts and X9, the ultra-compact qLMXB in 47 Tuc.

and $M_{625}=13.7$, respectively) than the 47 Tuc neutron-star qLMXBs (M_{625} between ~ 6.5 and ~ 8.8 , see Fig. 3). It is unlikely that similar systems⁷ are also present in 47 Tuc but have been missed; while in the optical they lie below the sensitivity of the *HST* data, they would have been easily detected by *Chandra*. For uncrowded sources, the Heinke et al. (2005b) 47 Tuc source catalogue is complete down to $L_X \approx 8 \times 10^{29}$ erg s⁻¹, whereas $L_X \approx 2 \times 10^{32}$ erg s⁻¹ for 44e (Henleywillis et al. 2018) and $L_X \approx 8 \times 10^{31}$ erg s⁻¹ for U24 (Bogdanov et al. 2010).

In the optical, the counterparts of X4 and X5 and the likely counterpart to X7 lie relatively close to the main sequence and show $H\alpha$ excess emission. This implies that the mass donors in these systems are non-degenerate, H-rich main-sequence stars. For X5, the non-degenerate nature of the secondary already followed directly from the known orbital period and eclipse light curve. For X7, the properties of the suggested counterpart are consistent with earlier conclusions from fitting X7’s X-ray spectrum. Unfortunately, the counterpart of W17 is not detected in $H\alpha$ and the nature of the donor remains unknown. Based on the large value of the lower limit on the X-ray-to-optical flux ratio, Edmonds et al. (2003b) identified W17 as a likely qLMXB. Our limit on the flux ratio from the simultaneous data (see Table 2 and discussion below) confirms this view. While we still cannot say with certainty whether X4 is a qLMXB or not, the properties of the counterpart to X4 (modest blue optical colour like X5 and X7, high flux ratio) make the case for X4 being a qLMXB stronger.

In a diagram of X-ray luminosity versus X-ray colours, X5 and X7 stand out as soft luminous sources in the cluster (see Fig. 14, adapted from Heinke et al. (2005b)). The more actively accreting

ultra-compact LMXB X9 is comparably bright, but has a harder spectrum. Classification based on X-ray luminosity and colours alone becomes more challenging for the less luminous sources X4, W17 and W37 (which could be classified as a qLMXB thanks to its X-ray light curve) because members of other source classes can reach similar luminosities. A case in point is X10 (also known as V3 or W27), which is also a bright soft source. X10 was classified as a probable magnetic CV based on its X-ray spectrum and periodic (4.67 hr) X-ray light curve (Heinke et al. 2005b; Bao et al. 2023) that are both typical for its source class.

Taking into account the properties of the optical or NUV counterparts helps to tell source classes apart. The known 47 Tuc CVs and qLMXBs span similar ranges in absolute magnitude (see Figs. 3 and 4) and excess $H\alpha$ emission (see Fig. 7). The CVs, however, have counterparts that tend to be bluer than the qLMXB counterparts. In particular in the optical R_{625} versus $B_{435} - R_{625}$ CMD, the counterparts of X4, X5 and X7 are not far offset from the blue of the main sequence. In other words, the relative contribution of an accretion disk or stream (and in addition, for some CVs, the emission of the white dwarf itself) to the combined light is more pronounced for CVs.

An often-used criterion for source classification is the ratio of the X-ray flux to optical flux, which is highest for qLMXBs, followed in order by CVs and ABs (Verbunt et al. 2008). This can be understood based on the different origins of the X-rays: emission from the heated surface of the compact object and accretion in qLMXBs and CVs (and from a shock region in magnetic systems) versus coronal activity of the rapidly rotating stars in a close binary of main-sequence and/or sub-giant stars. Neutron stars and black holes have the deepest potential wells and give rise to the highest accretion-powered X-ray luminosities. Edmonds et al. (2002b) demonstrated the diagnostic power of the X-ray-to-optical flux ratio for the classified *Chandra* sources in 47 Tuc. Since our 2002 *Chandra* and *HST* GO 9281 observations were taken simultaneously, the resulting flux ratios address concerns stemming from the X-ray and optical data being taken at different epochs. For example, Edmonds et al. (2002b) found that X5 and X10 have similar flux ratios but cautioned that since X10 is highly variable both in X-rays and in the optical, its actual F_X/F_{opt} value could be lower. The filled symbols in Fig. 15 show the X-ray fluxes from the 2002 *Chandra* observation against the GO 9281 F435W fluxes F_{435} (converted to unabsorbed absolute magnitudes)⁸. We include the securely identified CVs from Rivera Sandoval et al. (2018) but omitted W23 and W299 that have other candidate counterparts in the error circle, turning their reported X-ray luminosities (Heinke et al. 2005b) into upper limits. We find that $F_X/F_{435} \approx 1.4$, the flux ratio for X10 is somewhat lower than that of X5 (~ 1.7), but still not far off, even for the simultaneous fluxes. The high flux ratio for X10 can be explained by its nature as a magnetic CV: due to the high magnetic field of the white dwarf, there is no accretion disk in the system to contribute to the blue optical flux. Furthermore, we find that W51 is also relatively bright in X-rays compared to its optical flux. This may be due to the large flare produced by W51 in the 2002 *Chandra* observations (Heinke et al. 2005b, Fig. 6), which substantially increased its average flux; in the 2000 *Chandra* observations, its average flux was 5.7

⁷ with X-ray spectra dominated by a thermal component; note that a number of qLMXBs show a dominant non-thermal component (Campana et al. 2002; Jonker et al. 2004; Wijnands et al. 2005); such systems could be confused with CVs even in 47 Tuc (cf. Miller-Jones et al. 2015).

⁸ Note that in this figure, X-ray fluxes in the 0.5–6 keV band from the 2002 *Chandra* data are plotted (based on Table 2 in Heinke et al. 2005b). The corresponding X-ray-to-optical flux ratios may be different from those in Table 2, which were computed for specific (partial) ObsIDs or for a different epoch.

times lower (which would bring W51 more in line with other CVs in 47 Tuc). We do not understand the nature of this flare.

In order to try to further separate the qLMXBs and CVs, we make use of the finding that in the optical the qLMXB counterparts tend to lie closer to the main sequence than the CV counterparts. We turn this offset into an *excess* blue flux $F_{435,\text{exc}}$ in the following way. We assume that all the light in the F625W band is contributed by a main-sequence secondary. In an isochrone (age 11 Gyr, $Z=0.004$) generated with the PARSEC code (Bressan et al. 2012)⁹, we look up the corresponding B_{435} magnitude for such a star. The excess blue flux $F_{435,\text{exc}}$ is found by the difference between the observed B_{435} magnitude of the counterpart and the (theoretical) secondary-star flux. This is likely a lower limit to the excess blue flux, as the accretion flow may also contribute light in the redder filters. But it does give us an upper limit on $F_X/F_{435,\text{exc}}$ and combined with the value of F_X/F_{435} this delineates the range inside which the true value of $F_X/F_{\text{blue,exc}}$ should lie. As can be seen in Fig. 15, the distinction between the CVs and qLMXBs becomes more pronounced when considering the excess blue flux.

Using the excess blue fluxes versus X-ray fluxes, we see three groups in Fig. 15. At $\log F_X/F_{435,\text{exc}} > 2.0$, only qLMXBs are seen. Between $1.5 < \log F_X/F_{435,\text{exc}} < 2.0$, we see a qLMXB without NS surface emission (X9, likely a black hole qLMXB) and a CV without an optically bright accretion disk (X10, a polar CV). We also find W51 here, which is classified as a CV, but has a higher $F_X/F_{435,\text{exc}}$ than either X9 or X10, spurring us to speculate that W51 might be a magnetic CV or a hidden qLMXB (with a dominant nonthermal X-ray spectral component). Then at $\log F_X/F_{435,\text{exc}} < 1.5$, we see only CVs.

As a final note, we point out that the (likely) optical/NUV counterparts to X4, X5, X7 and W17 lie well within the error circles (Fig. 1). Since the radii of these error circles are dominated by the X-ray errors, this suggests that the prescription by Hong et al. (2005) for the 95% positional uncertainty on the *Chandra* positions overestimates the actual uncertainties. For the five sources that we consider here, we have also computed the X-ray errors using the formula in Kim et al. (2007). We find that for these bright sources the resulting 95% X-ray errors are about 3–5 times smaller than the Hong errors. The optical/NUV counterparts lie very close to, or within, the Kim error radii. We suggest that for future studies of bright *Chandra* sources, the use of the Kim errors is more appropriate as they eliminate many astrometric counterparts that would otherwise fall inside the (larger) error circles.

6 CONCLUSIONS

We have performed a detailed study of three certain (X5, X7 and W37) and two likely (X4 and W17) qLMXBs in 47 Tuc using simultaneous *Chandra* and optical *HST* data, complemented with non-contemporaneous optical and NUV *HST* data. We have discovered a blue and variable NUV counterpart to W17. The emission of a nearby bright star overwhelms this star in the optical. For X7, we suggest that the star N1, a previously identified astrometric match to this source, is the likely true counterpart. Since N1 looks like a main-sequence star, the atmosphere of the neutron star is probably H-rich. N1 has blue colours (in particular in the NUV), shows a modest $H\alpha$ excess and enhanced variability in U_{300} . These properties point at the presence of an accretion disk, but at the same time

X7 has not shown any signs of accretion in X-rays. We suggest that either gas from the disk has not reached the neutron star (yet), or that the power-law component associated with accretion is overwhelmed by the soft X-ray emission. We find a possible NUV counterpart for W37 but deeper higher-resolution imaging is needed to investigate the association with the X-ray source.

We have investigated the properties of the known optical/NUV counterparts to X4 and X5. For X4, we find that the simultaneous X-ray and optical light curves confirm that the X-ray variability is driven by changes in the accretion rate. In X5, minima in the optical and NUV light curves accompany the X-ray eclipses. The simultaneous X-ray and optical data suggest that the regions in the binary system that give rise to the blue and $H\alpha$ excess emission are obscured together with the X-rays. We find evidence for long-term variations in the optical from comparing our light curves with those taken about three years earlier.

Overall, based on the smaller blue (F435W) excess fluxes for $X4_{\text{opt}}$, $X5_{\text{opt}}$, and $X7_{\text{opt}}$ compared to the CV optical counterparts, we conclude that the accretion disks in the 47 Tuc qLMXBs are less prominent than in CVs. This makes the ratio of X-ray flux to excess blue optical flux a powerful discriminator between CVs and qLMXBs.

ACKNOWLEDGEMENTS

The authors thank R. Gilliland for providing GO 8267 light curves. This work is supported by Chandra grant GO3-4033A. This work made use of data from ESO telescopes obtained from the ESO/ST-ECF Science Archive Facility. CH is supported by NSERC Discovery Grants RGPIN-2016-04602 and RGPIN-2023-04264.

DATA AVAILABILITY

The *Chandra* data used in this work are available in the *Chandra* Data Archive at <https://cxc.harvard.edu/cda>. The *HST* data used in this work can be retrieved from the Mikulski Archive for Space Telescopes (MAST) Portal at <https://mast.stsci.edu/search/ui/#/hst>.

REFERENCES

- Albrow M. D., Gilliland R. L., Brown T. M., Edmonds P. D., Guhathakurta P., Sarajedini A., 2001, *ApJ*, 559, 1060
- Alcock C., Illarionov A., 1980, *ApJ*, 235, 534
- Anderson J., et al., 2008, *AJ*, 135, 2055
- Bahramian A., Heinke C. O., Degenaar N., Chomiuk L., Wijnands R., Strader J., Ho W. C. G., Pooley D., 2015, *MNRAS*, 452, 3475
- Bahramian A., et al., 2017, *MNRAS*, 467, 2199
- Bao T., Li Z., Cheng Z., 2023, *MNRAS*, 521, 4257
- Beccari G., De Marchi G., Panagia N., Pasquini L., 2014, *MNRAS*, 437, 2621
- Bernardini F., Cackett E. M., Brown E. F., D’Angelo C., Degenaar N., Miller J. M., Reynolds M., Wijnands R., 2013, *MNRAS*, 436, 2465
- Bhattacharya S., Heinke C. O., Chugunov A. I., Freire P. C. C., Ridolfi A., Bogdanov S., 2017, *MNRAS*, 472, 3706
- Bogdanov S., van den Berg M., Heinke C. O., Cohn H. N., Lugger P. M., Grindlay J. E., 2010, *ApJ*, 709, 241
- Bogdanov S., Heinke C. O., Özel F., Güver T., 2016, *ApJ*, 831, 184
- Bressan A., Marigo P., Girardi L., Salasnich B., Dal Cero C., Rubele S., Nanni A., 2012, *MNRAS*, 427, 127
- Brown E. F., Bildsten L., Rutledge R. E., 1998, *ApJ*, 504, L95

⁹ see also <http://stev.oapd.inaf.it/cgi-bin/cmd>

- Cackett E. M., Brown E. F., Miller J. M., Wijnands R., 2010, *ApJ*, **720**, 1325
- Cameron P. B., Rutledge R. E., Camilo F., Bildsten L., Ransom S. M., Kulkarni S. R., 2007, *ApJ*, **660**, 587
- Campana S., Colpi M., Mereghetti S., Stella L., Tavani M., 1998, *A&ARv*, **8**, 279
- Campana S., et al., 2002, *ApJ*, **575**, L15
- Campana S., Israel G. L., Stella L., Gastaldello F., Mereghetti S. 2004, *ApJ*, **601**, 474
- Chakrabarty D., et al., 2014, *ApJ*, **797**, 92
- Chen S., Richer H., Caiazzo I., Heyl J., 2018, *ApJ*, **867**, 132
- Church R. P., Strader J., Davies M. B., Bobrick A., 2017, *ApJ*, **851**, L4
- Cohn H. N., et al., 2010, *ApJ*, **722**, 20
- D'Angelo C. R., Fridriksson J. K., Messenger C., Patruno A., 2015, *MNRAS*, **449**, 2803
- D'Avanzo P., Campana S., Casares J., Israel G. L., Covino S., Charles P. A., Stella L., 2005, *A&A*, **444**, 905
- Deutsch E. W., Margon B., Anderson S. F., 2000, *ApJ*, **530**, L21
- Dolphin A. E., 2000, *PASP*, **112**, 1383
- Echiburú C. S., Guillot S., Zhao Y., Heinke C. O., Özel F., Webb N. A., 2020, *MNRAS*, **495**, 4508
- Edmonds P. D., Heinke C. O., Grindlay J. E., Gilliland R. L., 2002a, *ApJL*, **564**, L17
- Edmonds P. D., Gilliland R. L., Camilo F., Heinke C. O., Grindlay J. E., 2002b, *ApJ*, **579**, 741
- Edmonds P. D., Gilliland R. L., Heinke C. O., Grindlay J. E., 2003a, *ApJ*, **596**, 1177
- Edmonds P. D., Gilliland R. L., Heinke C. O., Grindlay J. E., 2003b, *ApJ*, **596**, 1197
- Ferraro F. R., Pallanca C., Lanzoni B., Cadelano M., Massari D., Dalessandro E., Mucciarelli A., 2015, *ApJ*, **807**, L1
- Gilliland R. L., et al., 2000, *ApJ*, **545**, L47
- Gonzaga S., Hack W., Fruchter A., Mack J., eds, 2012, *The DrizzlePac Handbook*
- Grindlay J. E., Heinke C., Edmonds P. D., Murray S. S., 2001, *Science*, **292**, 2290
- Haggard D., Cool A. M., Anderson J., Edmonds P. D., Callanan P. J., Heinke C. O., Grindlay J. E., Bailyn C. D., 2004, *ApJ*, **613**, 512
- Haggard D., Cool A. M., Davies M. B., 2009, *ApJ*, **697**, 224
- Hasinger G., Johnston H. M., Verbunt F., 1994, *A&A*, **288**, 466
- Heinke C. O., Grindlay J. E., Lloyd D. A., Edmonds P. D., 2003a, *ApJ*, **588**, 452
- Heinke C. O., Grindlay J. E., Lugger P. M., Cohn H. N., Edmonds P. D., Lloyd D. A., Cool A. M., 2003b, *ApJ*, **598**, 501
- Heinke C. O., Grindlay J. E., Edmonds P. D., 2005a, *ApJ*, **622**, 556
- Heinke C. O., Grindlay J. E., Edmonds P. D., Cohn H. N., Lugger P. M., Camilo F., Bogdanov S., Freire P. C., 2005b, *ApJ*, **625**, 796
- Heinke C. O., Rybicki G. B., Narayan R., Grindlay J. E., 2006, *ApJ*, **644**, 1090
- Heinke C. O., et al., 2014, *MNRAS*, **444**, 443
- Henleywillis S., Cool A. M., Haggard D., Heinke C., Callanan P., Zhao Y., 2018, *MNRAS*, **479**, 2834
- Hong J., van den Berg M., Schlegel E., Grindlay J., Koenig X., Laycock S., Zhao P., 2005, *ApJ*, **635**, 907
- Jonker P. G., Galloway D. K., McClintock J. E., Buxton M., Garcia M., Murray S., 2004, *MNRAS*, **354**, 666
- Katz J. I., 1975, *Nature*, **253**, 698
- Kim M., et al., 2007, *ApJS*, **169**, 401
- Koekemoer A., McLean B., McMaster M., Jenkner H., 2005, Technical report, Instrument Science Report ACS 2005-06. STScI
- Kononov D., Lacy C., Puzin V. B., Kozhevnikov V. P., Sytov A. Y., Lyaptsev A. P., 2017, in *The Golden Age of Cataclysmic Variables and Related Objects IV*. p. 31 ([arXiv:1607.00265](https://arxiv.org/abs/1607.00265)), doi:10.22323/1.315.0031
- Li J., Kastner J. H., Prigozhin G. Y., Schulz N. S., Feigelson E. D., Getman K. V., 2004, *ApJ*, **610**, 1204
- Linares M., 2014, *ApJ*, **795**, 72
- Lomb N. R., 1976, *Ap&SS*, **39**, 447
- Lugger P. M., Cohn H. N., Cool A. M., Heinke C. O., Anderson J., 2017, *ApJ*, **841**, 53
- Miller-Jones J. C. A., et al., 2015, *MNRAS*, **453**, 3918
- Nardiello D., et al., 2018, *MNRAS*, **481**, 3382
- Özel F., Freire P., 2016, *ARA&A*, **54**, 401
- Pallanca C., Dalessandro E., Ferraro F. R., Lanzoni B., Beccari G., 2013, *ApJ*, **773**, 122
- Pooley D., Hut P., 2006, *ApJL*, **646**, L143
- Pooley D., et al., 2003, *ApJ*, **591**, L131
- Qiao, E., Liu, B. F., 2018, *MNRAS*, **481**, 938
- Qiao, E., Liu, B. F., 2020, *MNRAS*, **492**, 615
- Qiao, E., Liu, B. F., 2021, *MNRAS*, **502**, 3870
- Rivera Sandoval L. E., et al., 2015, *MNRAS*, **453**, 2707
- Rivera Sandoval L. E., et al., 2018, *MNRAS*, **475**, 4841
- Romani R. W., 1987, *ApJ*, **313**, 718
- Rutledge R. E., Bildsten L., Brown E. F., Pavlov G. G., Zavlin V. E., 2002, *ApJ*, **578**, 405
- Salaris M., Held E. V., Ortolani S., Gullieuszik M., Momany Y., 2007, *A&A*, **476**, 243
- Sarajedini A., et al., 2007, *AJ*, **133**, 1658
- Scargle J. D., 1982, *ApJ*, **263**, 835
- Servillat M., Heinke C. O., Ho W. C. G., Grindlay J. E., Hong J., van den Berg M., Bogdanov S., 2012, *MNRAS*, **423**, 1556
- Shahbaz, T., González-Hernández, J. I., Breton, R. P., Kennedy, M. R., Mata Sánchez, D., Linares, M., 2022, *MNRAS*, **513**, 71
- Sirianni M., et al., 2005, *PASP*, **117**, 1049
- Steiner A. W., Heinke C. O., Bogdanov S., Li C. K., Ho W. C. G., Bahramian A., Han S., 2018, *MNRAS*, **476**, 421
- Testa V., et al., 2012, *A&A*, **547**, A28
- Tudor V., et al., 2018, *MNRAS*, **476**, 1889
- Verbunt F., van Kerkwijk M. H., in't Zand J. J. M., Heise J., 2000, *A&A*, **359**, 960
- Verbunt F., Pooley D., Bassa C., 2008, in Vesperini E., Giersz M., Sills A., eds, *International Astronomical Union Symposium no. 246 Vol. 246, Dynamical Evolution of Dense Stellar Systems*. pp 301–310 ([arXiv:0710.1804](https://arxiv.org/abs/0710.1804)), doi:10.1017/S1743921308015822
- Walsh A. R., Cackett E. M., Bernardini F., 2015, *MNRAS*, **449**, 1238
- Wijnands R., Heinke C. O., Pooley D., Edmonds P. D., Lewin W. H. G., Grindlay J. E., Jonker P. G., Miller J. M., 2005, *ApJ*, **618**, 883
- Wijnands, R., Degenaar, N., Armas Padilla, M., Altamirano, D., Cavecchi, Y., Linares, M., Bahramian, A., Heinke, C. O., 2015, *MNRAS*, **454**, 1371
- Zacharias N., Urban S. E., Zacharias M. I., Wycoff G. L., Hall D. M., Monet D. G., Rafferty T. J., 2004, *AJ*, **127**, 3043
- in't Zand J. J. M., van Kerkwijk M. H., Pooley D., Verbunt F., Wijnands R., Lewin W. H. G., 2001, *ApJ*, **563**, L41
- in't Zand J. J. M., et al., 2003, *A&A*, **406**, 233

APPENDIX A: REFINING THE ORBITAL PERIOD OF X5

The eclipses of X5 are total eclipses, averaging 2500 s long, which can be explained by the X-rays coming exclusively from the neutron star surface. Only occasional background photons fall within the eclipse. To provide the photon list, we extract lightcurves at the instrument time resolution (for ACIS, or 2.0 s for HRC) from barycentred event files. We use the 0.5–2 keV energy range for ACIS data (which includes most source photons, while reducing background) and a 1.0'' extraction region to create the lightcurves. We use ACIS observations from 2000 (ObsIDs 953, 955; Heinke et al. 2003a), 2002 (ObsIDs 2735–3386 in Table A1, described in §2.1), 2014 (ObsIDs 16527–15748, Bogdanov et al. 2016), and 2022 (ObsID 26229, PI Paduano), along with HRC observations in 2005–2006 (ObsIDs 5542–6240, Cameron et al. 2007).

The countrate from X5 is low enough (typically 0.1 counts/second, or lower) that we choose not to try to fit the eclipse with a specified function, nor to fit the ingresses and egresses, as when studying eclipses of bright LMXBs (e.g. in't Zand et al. 2003).

Instead, we find the best approach is to find the midpoint of each eclipse using the last photon recorded before the eclipse, and the first photon after it. The uncertainty in the eclipse midpoint is thus

$\sigma_{mid} = \sqrt{(\sigma_{in}^2 + \sigma_{out}^2)}/2$, where e.g. σ_{in} is the inverse of the measured counts in the 100 seconds up to the last photon. This requires some iteration, to identify likely background photons interrupting eclipses (we find only 14 such interlopers). We omit using eclipses if the continuum countrate is so low that the eclipse is substantially longer than average (>2700 s), or if we measure only an ingress or an egress. This leaves us with 35 complete and high-quality eclipses, spread from 2000 to 2022, with 20 observed during the 2005–2006 HRC data. The eclipse midpoints, and their associated errors, are given in Table A1, including three not used for our calculation, in units of TDB seconds since MJD_REF=50814.0 (barycentred).

We calculate the orbital period iteratively, using eclipses close in time to find the orbital period and its error, and then predict more distant eclipses, which then refine the orbital period and its error. If the error in the orbital period for the next eclipse is less than half an orbital period, we maintain cycle count.

We begin with ObsID 6238 in 2005, which has two well-measured eclipses, which give $P=31195 \pm 30$ s. We then extrapolate this solution 3 cycles to ObsID 5546, refining the period to $P=31204 \pm 7.5$ s, and continue similarly. We include the cycle count (from the 2nd eclipse of ObsID 6238) in Table A1. Using the full range of eclipses, we arrive at an orbital period solution for X5's X-ray eclipse midpoints, measured from MJD_REF=50814.0, of TDB=251975445(± 16)+ $n \times 31200.192(\pm 0.002)$ s, where n is an integer.

This paper has been typeset from a $\text{\TeX}/\text{\LaTeX}$ file prepared by the author.

ObsID	Midpoint ^a s	Offset s	Error s	Cycle Count
953	69610285	-38	26	-5845
955	69641492.5	-30	17	-5844
2735	149732465.5	50	17	-3277
2735	149763664*	48	33	-3276
2736	149794986.5*	170	119	-3275
2736	149826053	37	20	-3274
2737	149982022.5	5	15	-3269
2737	150013441*	223	376	-3268
3386	150044439	21	15	-3267
2738	150699598	-24	15	-3246
5542	251382640	-1	15	-19
5543	251507389	-53	17	-15
5544	251601060	17	15	-12
5544	251632237	-6	19	-11
5545	251725832	-11	21	-8
6237	251850633	-11	21	-4
6238	251944250	5	26	-1
6238	251975445	0	16	0
5546	252069066	20	15	3
6230	252193857	11	21	7
6231	252287482	35	38	10
6231	252318628	-19	20	11
6232	252412263	15	19	14
6233	252599456	7	25	20
6233	252630661	12	25	21
6233	252661850	1	20	22
6235	252755438	-12	21	25
6236	252880266	15	17	29
6239	253005058	7	13	33
6240	253098648	-4	13	36
16527	526287538	5	38	8792
16527	526318725	-8	17	8793
15747	526693116	-20	18	8805
15747	526724336	0	20	8806
16529	527691504.5	-37	19	8837
15748	528627523.5	-24	38	8867
16528	539297989.5	-24	20	9209
26229	759602543.5	-25	40	16270

Table A1. X-ray eclipse midpoints. Offsets are the differences between the observed eclipse midpoint and our calculated ephemeris (observed-calculated times). Errors are the estimated uncertainty in the eclipse midpoint, based on the countrate in the earlier/later 100 seconds. ^a TDB barycentred time, in seconds, since MJD_REF=50814.0. *-Not used in our calculations.